ULF foreshock under radial IMF: THEMIS observations and global kinetic simulation Vlasiator results compared

M. Palmroth[1], M. Archer[2,3], R. Vainio[4], H. Hietala[2], Y. Pfau-Kempf[1,5], S. Hoilijoki[1,5], O. Hannuksela[1,5], U. Ganse[5], A. Sandroos[1], S. von Alfthan[6], and J. P. Eastwood[2],

Corresponding author: Minna Palmroth, Finnish Meteorological Institute, Helsinki, Finland. (minna.palmroth@fmi.fi)

[1]Finnish Meteorological Institute, Helsinki, Finland

[2]The Blackett Laboratory, Imperial College London, London, UK

[3]Queen Mary University of London, London, UK

[4]University of Turku, Turku, Finland

[5]University of Helsinki, Helsinki, Finland

[6]CSC - IT Center for Science, Espoo, Finland

Abstract.

For decades, monochromatic large-scale ultra low frequency (ULF) waves with a period of about 30 seconds have been observed upstream of the quasi-parallel bow shock. These waves typically propagate obliquely with respect to the interplanetary magnetic field (IMF), while the growth rate for the instability causing the waves is maximized parallel to the magnetic field. It has been suggested that the mechanism for the oblique propagation concerns wave refraction due to the spatial variability of the suprathermal ions, originating from the $\mathbf{E}\times\mathbf{B}$ drift component. We investigate the ULF foreshock under a quasi-radial IMF with Vlasiator, which is a newly developed global hybrid-Vlasov simulation solving the Vlasov equation for protons, while electrons are treated as a charge-neutralizing fluid. We observe the generation of the 30-second ULF waves, and compare their properties to previous literature and multipoint THEMIS spacecraft observations. We find that Vlasiator reproduces the foreshock ULF waves in all reported observational aspects. We conclude that the variability of the density and velocity of the reflected backstreaming ions determines the large-scale structure of the foreshock, which affects the wave frequency, wavelength and oblique propagation. We conclude that the wave refraction may also be at work for radial IMF conditions, which has earlier been thought of as an exception to the refraction mechanism due to the small $\mathbf{E}\times\mathbf{B}$ drift component. We suggest that additional refraction may be caused by the large-scale spatial variability of the density and velocity of the backstreaming ions.

1. Introduction

The interplanetary magnetic field (IMF) divides the Earth's bow shock into roughly two regions according to whether the angle between the bow shock normal and the IMF (θ_{Bn}) is more or less than 45° degrees. In the former (latter) case, the shock is called quasi-perpendicular (quasi-parallel). At the quasi-parallel shock, solar wind particles streaming towards the bow shock can reflect at the shock surface and stream back upstream along the IMF, forming a foreshock. The foreshock exhibits several kinds of waves and wave packets, for example 1 Hz waves, 3-second waves, sinusoidal and nearly sinusoidal 30-second waves, and shocklets and discrete wave packets [e.g., *Hoppe et al.* 1981; *Russell and Hoppe*, 1983; *Russell et al.* 1987; *Greenstadt et al.* 1995].

Paschmann et al. [1980] investigated the ion distribution functions within the foreshock, and explained the energies of the backstreaming particles with a model that depends on the angles between the IMF, bow shock normal and the solar wind, and compared to 18 events observed by the ISEE spacecraft. Using 2-dimensional ISEE spacecraft data, *Paschmann et al.* [1981] characterized and named a number of different ion distributions in the foreshock. They noted that the reflected populations have a fast beam well separated from the solar wind core population and have a strong temperature anisotropy. On the other hand *Paschmann et al.* [1981] characterized diffuse populations occupying a larger area in the phase space, where solar wind core population can be encapsulated by the diffuse ions. In between these two population types, *Paschmann et al.* [1981] observed transitions of intermediate populations, which led them to suggest that diffuse populations result from pitch angle scattering of the reflected beam populations.

In the category of large-amplitude 30-second waves, both left-handed and right-handed polarizations with similar frequencies, and wavelengths have been observed [*Hoppe et al.*, 1981]. The left-handed waves are thought to originate from ion/ion beam instabilities, while the right-handed polarized waves may be caused by non-resonant firehose instability or by left-handed Alfvén/ion resonant instability [*Gary*, 1993]. *Russell et al.* [1987] investigated the foreshock waves using two spacecraft, and found that the wave characteristics depend on where in the foreshock they are detected. The properties of the left-handed nearly sinusoidal waves are more monochromatic and more weakly compressive closer to the ion foreshock boundary [*Sibeck et al.*, 2008] (later called the foreshock compressional boundary [*Omidi et al.*, 2009; *Rojas-Castillo et al.*, 2013]), while deeper in the foreshock they become more compressional and can steepen into shocklets [*Greenstadt et al.*, 1995; *Hoppe and Russell*, 1983]. This paper concentrates on the quasi-monochromatic left-handed 30-second ultra low frequency (ULF) waves, thought to be due to the right-hand resonant ion-ion beam instability [*Gary*, 1993] arising from the backstreaming ion interaction with the solar wind population.

The 30-second waves were first observed by *Greenstadt et al.* [1968] and *Fairfield* [1969], and their characteristics have since been the subject of many studies. Although they are called the 30-second waves for their period, a considerable spread in the period has been observed, ranging from 10 s to ∼55 s [*Eastwood et al.*, 2005a]. The period depends on the IMF strength and cone angle [*Takahashi et al.*, 1984] that ranges from radial IMF (0°) to the typical Parker spiral condition (45°) and beyond. The waves are right-handed in the plasma frame, and elliptically polarized [*Le and Russell*, 1994]. The wavelength is of the order of an Earth radius (R_E) parallel to magnetic field [*Le and Russell*, 1994], while in the perpendicular direction the wave size can be 8-18 R_E [*Archer et al.*, 2005]. The distribution functions associated with the waves show often either a narrow field-aligned beam (closer to the foreshock compressional boundary), whereas otherwise the distributions are mostly observed as intermediate, diffuse or gyrophase bunched [*Fuselier et al.*, 1986; *Meziane et al.*, 2001; *Mazelle et al.*, 2003; *Kempf et al.*, 2015].

One intriguing factor related to the 30-second waves is that while the growth rate of the instability giving rise to the waves maximizes in the direction parallel to the ambient magnetic field [*Gary*, 1993], the waves are observed to propagate obliquely, typically at about 20° with respect to the background magnetic field [*Le and Russell*, 1994; *Eastwood et al.*, 2005b; *Hsieh and Shue*, 2013]. *Eastwood et al.* [2004] showed that the wave deflection occurs in the plane defined by the magnetic field and the solar wind velocity direction. Several attempts exist to explain the oblique propagation: *Winske et al.* [1985] proposed that the right-hand resonant instability due to gyrating ions is an important mechanism for wave growth near the bow shock, while *Omidi et al.* [1994] and *Killen et al.* [1995] showed that the beam-ring ion distributions may excite oblique waves. *Hada et al.* [1987] proposed a mechanism for the oblique propagation based on refraction. In their mechanism, waves are generated parallel to the magnetic field by instabilities due to the presence of the backstreaming ions. As the waves are advected downstream with the solar wind, they may encounter a nonuniform refractive index due to the spatial variation of the backstreaming ions. To be refracted, waves need to have a wave vector and a group velocity component along the gradient of the refractive index. For non-zero cone angles, the $\mathbf{E}\times\mathbf{B}$ drift of the beam ions leads to variations in the beam structure that are not aligned with the field and solar-wind advection transports the wave across the structured beam. Therefore, refraction of waves initially generated in the parallel direction should occur. However, under radial IMF conditions the group velocity of parallel-propagating waves is along the field lines. If the structure of the beam varies across the field only due to the $\mathbf{E}\times\mathbf{B}$ drift, oblique waves would be present only for nonzero cone angles. Several observations state the opposite, and oblique propagation occurs even under quasi-radial IMF [*Eastwood et al.*, 2005b; *Hsieh and Shue*, 2013], suggesting the oblique wave propagation is still not fully understood. Observations indicate that the waves bend in many directions, while the oblique propagation angle is not correlated with the wave frequency or polarization, the strength of the IMF, or the solar wind speed [*Eastwood et al.*, 2005b; *Hsieh and Shue*, 2013].

Modelling the foreshock requires a simulation representing kinetic physics. With limited computational resources in the past, local simulations have therefore prevailed [e.g., *Winske*, 1985], while the global features of the shock have been out of reach to magnetohydrodynamic simulations [e.g., *Janhunen et al.*, 2012] due to insufficient ion-scale physics. Only during the past decade, computational resources have increased such that it has been possible to investigate the global features of the foreshock. The most common way to model the foreshock is by hybrid particle-in-cell methods (hybrid-PIC), where ions are particles launched to the simulation, while electrons are modeled as a charge-neutralizing fluid [*Omidi et al.*, 2005; *Blanco-Cano et al.*, 2006, 2009; *Karimabadi et al.*, 2014]. These simulations have typically modeled two-dimensional setups with a down-scaled geomagnetic dipole. Despite the consequent uncertainties in the scale sizes of the system and even though the ion distribution functions have suffered from the limited number of particles used in the simulation, this approach has been able to reproduce the wave characteristics. *Blanco-Cano et al.* [2009] investigated the ULF waves under radial IMF conditions, but did not identify a mechanism for the oblique propagation angle. Recently, a new global approach complementary to the hybrid-PIC based on the hybrid-Vlasov approach has been developed [*Palmroth et al.*, 2013; *von Alfthan et al.*, 2014]. This approach is computationally more demanding than the hybrid-PIC and it does not track the origin of particles inherently. However, the hybrid-Vlasov method produces an improved representation of the ion distribution function [*Pokhotelov et al.*, 2013; *Kempf et al.*, 2015] without the numerical noise, and it is able to model the system without scaling the geomagnetic dipole strength, leading to correct scale sizes of the system.

This article investigates the foreshock ULF waves under the special condition of nearly radial IMF, using the Vlasiator simulation in a two-dimensional setup. The target is first to investigate the ULF wave characteristics, and to validate the simulation results by comparing to earlier literature and experimental data recorded by THEMIS spacecraft [*Angelopoulos*, 2008]. Second, the almost radial IMF introduces an opportunity to investigate the oblique propagation of the waves. The article is structured as follows: First, we briefly describe the Vlasiator simulation and the run setup for the radial IMF case. We then investigate the ULF wave characteristics within the foreshock, and compare to earlier literature. In Section 4 compare the characteristics to THEMIS observations. Finally, we discuss the problem of oblique propagation and present an initial idea for the oblique propagation mechanism under radial IMF, informed by the Vlasiator simulation results.

2. Model Description

Vlasiator is a newly developed global hybrid-Vlasov model, where protons are described by the full distribution function $f(\mathbf{r}, \mathbf{v}, t)$ in the phase space, and electrons are treated as a charge-neutralizing fluid [*von Alfthan et al.*, 2014]. This approach neglects electron kinetic effects but includes the ion kinetic effects without the numerical noise present in hybrid-PIC methods, in which the distribution function noise is typically controlled by increasing the number of launched particles. The time-evolution of $f(\mathbf{r}, \mathbf{v}, t)$ is given by the Vlasov equation, propagated by a fifth-order accurate semi-Lagrangian approach [*Zerroukat and Allen*, 2012; *White and Adcroft*, 2008]. The electromagnetic fields are solved using Maxwell's equations neglecting the displacement current in the Ampère-Maxwell law. Maxwell's equations are supplemented by Ohm's law, including the Hall term neglected in previous Vlasiator versions [*Palmroth et al.*, 2013; *von Alfthan et al.*, 2014; *Kempf et al.*, 2015]. The closure scheme, the numerical approach and the parallelization description can be found in *von Alfthan et al.* [2014], while newer additions to the code include the Semi-Lagrangian solver replacing the older Finite Volume Method, and the Hall term in Ohm's law.

Vlasiator was used to simulate an event with almost radial IMF conditions. The time-stationary solar wind conditions are given in Table 1. Due to computational resource limits, in this run the simulation box is 5D, where the ordinary space is solved in the ecliptic XY plane of the Geocentric Solar Ecliptic (GSE) coordinate system, while each ordinary space cell includes a separate velocity space self-consistently coupled to the ordinary space. The box size in ordinary space in this run is from -7 R_E to 60 R_E in X, and ± 30 in Y, with a resolution of 227 km, while the ion inertial length in this run is 125.4 km (see Table 1). The velocity space resolution is 30 km/s. The solar wind conditions are introduced at the sunward wall of the simulation box, while at other boundaries copy conditions are employed, i.e., the full distribution function is copied from the nearest spatial cell that is inside the simulation domain. Periodic boundary conditions are applied in the Z direction of the ordinary space. The inner edge of the magnetospheric domain is set at a circle with a radius of 5 R_E, from where the dipole field is mapped to the ionosphere, which currently is a perfect conductor. Vlasiator uses the actual unscaled geomagnetic dipole strength as a boundary condition.

3. Modeling results

Figure 1a shows an overview of Vlasiator modeling of plasma density in the ecliptic plane under quasi-radial IMF conditions with 5° cone angle. The color-coding is taken from one time instant in the run, representing 500 s from the beginning of the run, by which time the foreshock has already developed. Magnetosheath is shown as red, and is bound on its inner and outer edges by the magnetopause and bow shock, respectively. The black dots indicate the positions of virtual spacecraft for which time series data are taken from the simulation for later analysis, while the grey dot is the position of the virtual spacecraft for which data are given in Fig. 2. The red dots refer to Section 4 and are discussed there. Figure 1b shows an example of the distribution function at position $[X, Y]$ = [18, -5] R_E, as a cut of the velocity XZ plane.

Figure 1a indicates that the foreshock wave field is visible approximately at 10 R_E to 50 R_E in the X and about ±15 R_E in Y, while at later time instants the wave field extends to the edge of the simulation domain in $+X$. The plasma density shows clear oblique wave fronts bent in many directions with respect to the ambient IMF. The wave fronts appear generally structured around and along two ‘backbones’ or ‘spines’ extending along the X axis, at approximately $Y = -12$ and 2 R_E. Further, there is a clear difference in the oblique angle between the edges of the foreshock and the central foreshock. The solar wind advects the wave fronts towards the bow shock surface (as shown in the animation given as supplementary material to this paper). Around $[X, Y] = [20, 0]$ R_E the wave fronts show isolated areas of decreased density in comparison to the surrounding plasma, which appear to be consistent with the known properties of foreshock cavitons [*Blanco-Cano et al.*, 2011]. Figure 1b presents two plasma populations, the core solar wind flowing with the solar wind velocity towards the Earth, and the population reflected at the bow shock, streaming along the positive X with approximately the speed of 500 km/s. For a more detailed discussion of the distribution function structure, see *Kempf et al.* [2015].

Figure 2 shows temporal data from the virtual spacecraft positioned at $[X, Y] = [18, -5]$ R_E (cf. Fig. 1). Panels 2a-e show density, magnetic field intensity $|B|$, and x, y, and z components of the magnetic field, respectively, as a function of time in the simulation. The density fluctuations are about 10-15% of the ambient solar wind. The fluctuations before about $t = 520$ s are more evenly structured, while after $t = 520$ s the virtual spacecraft is co-located with a region where the wave frequency and density amplitude increases. This region is the outskirt of the caviton-like structure visible in Fig. 1. The waves are compressive, as they also have a magnetic depression of about 10-20% of the ambient magnetic field intensity (panels 2b-e), in line with e.g., *Le and Russell* [1994]; *Eastwood et al.* [2002]. The caviton-like structure exhibits smaller magnetic field fluctuations, consistent with typical features related to cavitons [*Blanco-Cano et al.*, 2011]. The Fourier transform of the magnetic field fluctuations (not shown) reveals clear peaks in the power spectral density at frequencies of 0.023 Hz, 0.025 Hz, 0.025 Hz, and 0.023 Hz as deduced from a Fourier transform using B_x, B_y, B_z, and B respectively, corresponding to wave periods of 40 s and 43.5 s. For a cone angle of 5°, an estimation based on empirical observations should be about 0.037 Hz, corresponding to a period of 27 s [*Takahashi et al.*, 1984].

Figure 3a shows a histogram of the wave periods, evaluated using the virtual spacecraft time series of the magnetic field z component. Even though there are 34 virtual spacecraft from which temporal data are analyzed, the Fourier spectrogram may exhibit more peaks at a single position, and hence there are more than 34 entries in Fig. 3a (only peaks above 40% of the maximum power spectral density are considered here). Figure 3a shows that most of the foreshock waves have a period of 30-40 s, while there are also longer and shorter period waves present. This is consistent with *Eastwood et al.* [2005a]. Other components of the magnetic field and the magnetic field intensity yield similar results for the period histogram.

Figure 3b presents a histogram of the angle of propagation of the foreshock wave fronts. The angle is calculated using the virtual spacecraft magnetic field time series as input to a minimum variance analysis, where the minimum variance direction gives an estimate of the wave vector $\mathbf{k}$ [e.g., *Hoppe et al.,* 1981]. The dot product of $\mathbf{k}$ with the ambient IMF direction gives θ_{kB}, which is the angle at which the wave front propagates with respect to the magnetic field. Figure 3b indicates that θ_{kB} varies mostly between 0° and 20°, peaks below 10°, while larger angles are not absent. Again, this is in good agreement with *Eastwood et al.* [2005b], reporting that even with cone angles reaching radial IMF conditions the propagation angle is approximately between 5° and 20° (see Figure 5 of *Eastwood et al.* [2005b]).

Figure 4 presents the foreshock wave field as a color plot of the B_z component representing an Alfvénic disturbance. The figure (like Fig. 1) is a snapshot at 500 s from the beginning of the simulation. Overlaid with B_z are contours of B_y that illustrate the waves. Black vectors are the x and y components of the minimum variance direction representing the wave front orientation. The minimum variance direction is calculated from the temporal magnetic field data of the virtual spacecraft using all simulation data during which the virtual spacecraft is within the foreshock proper (see Fig. 1). The colored straight lines through the dusk, central and dawn side of the foreshock refer to Figure 6.

Let us first scrutinise the wave fronts using the color plot and the contours. Generally, the foreshock waves have oblique orientations tilted towards both positive and negative Y axis. The waves being born at the largest distances from the bow shock are roughly perpendicular to the magnetic field, before they are advected towards the bow shock surface. Typically, the wave fronts are bent towards the positive (negative) Y axis near the foreshock edges at positive (negative) Y. Near the bow shock surface closer than approximately 20 R_E, the wave front orientations become more disorganized.

Figure 4 illustrates that the minimum variance direction is generally a good indication of the wave front orientation in the foreshock. In 25 cases out of 34, the intermediate to minimum eigenvalue ratio of the minimum variance analysis is larger than 8, while in two cases it is between 1.8 and 2, indicating that generally the minimum variance analysis can be trusted [*Eastwood et al.*, 2002]. Furthermore, near the bow shock surface, the waves are not as coherently oriented as further upstream, and hence the minimum variance direction also slightly deviates from the wave front normal direction at the corresponding virtual spacecraft positions.

Figure 5 illustrates the wave period and propagation angle characteristics more quantitatively as a function of location in the foreshock. Panel 5a shows the wave period as a function of distance along the X axis, as determined by Fourier analysis of the virtual spacecraft B_z measurements. The wave periods from time series that have been observed in the dusk (dawn) side of the foreshock have been colored red (blue), respectively. The wave periods have a larger variation near the bow shock most probably due to more turbulent conditions there, while further upstream in the foreshock the waves are more consistently of the same period ($30 - 40$ s). The waves in the dusk side foreshock have shorter periods than waves in the dawn foreshock.

Figure 5b shows the wave propagation angle with respect to the IMF direction as measured from the minimum variance analysis. Consistent with the visual analysis in Fig. 4, there is a clear break point in the propagation angle at 23 R_E. Upstream of this distance, the wave propagation angles vary considerably. At 23 R_E, the wave propagation angle is the smallest throughout the foreshock, while downstream of this distance the propagation angle spreads again, although this is not as pronounced as in the upstream area. The dawn side propagation angles tend to be slightly more oblique throughout the foreshock compared to the dusk side propagation angles. Based on Fig. 5a-b we conclude that the waves in the dusk foreshock appear shorter in period and their propagation angle is more aligned with the IMF, while the dawn foreshock waves have a larger period and a larger propagation angle with respect to the IMF.

Figure 6a-c shows the B_z component evaluated at the dusk, central and dawn sides of the foreshock, at lines through the ordinary space illustrated with red, green and blue colors, respectively, in Fig. 4. Panels 6a-c indicate fully developed wave activity throughout the foreshock, with more evenly structured waves further upstream, and more deformed waves near the bow shock surface. There are high amplitude perturbations with apparently shorter wavelength which appear near the bow shock surface. Especially close to the dawn edge of the foreshock, the wave amplitudes are relatively smaller near the bow shock surface and far upstream, while larger amplitudes are observed at distances of about 30 R_E from the shock surface. In the central foreshock, the wave amplitudes are pronounced throughout, with the exception of the far upstream area. The waves appear to grow more easily at the edges of the foreshock, while the waves in the central foreshock appear to grow at slightly smaller distances; this can also be seen in the color-coding in Fig. 4.

To evaluate the wavelength, in Fig. 6d we plot the distance between the wave peak amplitudes along each line, using the same color-coding, i.e., the red dots show the distance between the peak amplitudes on the red curve (Fig. 6a), which is a cut through the dusk side of the foreshock (see Fig. 4). Note that the wavelength is measured along the spatial cut that is not exactly parallel to the individual wave **k**. Figure 6 illustrates that the wavelengths vary approximately between 1 to 4 R_E, in accordance with *Le and Russell* [1994]. The wavelengths decrease towards the shock surface. In particular we note that the wavelengths increase with increasing distance from the shock at the edges of the foreshock, while in the central foreshock the effect is not as clear.

In the perpendicular direction, the wave sizes depend on the distance from the bow shock. Figure 4 indicates that near the bow shock surface the lengths of the wave fronts are about 5 R_E and upwards in the perpendicular direction. Further upstream, some waves fronts can extend across the entire foreshock and hence the perpendicular scale e.g., at $X = 25$ R_E can be over 20 R_E. Furthest upstream, the wave perpendicular scales are again closer to 5 R_E. *Archer et al.* [2005] report wave sizes from 8 to 18 R_E perpendicular to **k**, in agreement with the results here.

Finally, we investigate the polarization of the foreshock wave field. Figure 7 shows the wave field polarization using data from the virtual spacecraft positioned at [18, -5] R_E (see Fig. 1), for the time period $255.5 - 474.5$ s (see Fig. 2), i.e., neglecting the waves associated with the region of caviton-like structures visible in Fig. 1. For evaluating the polarization, we define $\Delta\mathbf{B}$ by removing the background magnetic field from the virtual spacecraft measurement. Then, we define a projection of the magnetic field in the XY plane as a dot product of the $\Delta\mathbf{B}$ with a unit vector in the XY plane, defined as the cross product of the Z axis and the wave normal from the minimum variance analysis. Figure 7 shows the wave magnetic field in the XY plane against the wave magnetic field in the Z direction such that the direction towards the viewer is the wave **k** in the direction of the IMF, while the circle indicates the start of the time series. The polarization is elliptical and left-handed in the virtual spacecraft frame with respect to the magnetic field direction. However, polarization is defined in the plasma rest frame, and if the wave vector and the advection velocity are anti-parallel, as is the case with the foreshock waves, the handedness of the waves flips, making the intrinsic polarization of the waves in Fig. 7 elliptical and right-handed. This is again in accordance with several previous papers, e.g., *Hoppe et al.* [1981]; *Le and Russell* [1994]; *Eastwood et al.* [2002, 2005a].

4. Observations

Next, we wish to investigate, using spacecraft observations, how the Vlasiator modeling results correspond to actual foreshock wave properties. We searched the THEMIS 2008 dayside season for periods with similar solar wind conditions whereby multipoint spacecraft observations in the foreshock were available. This resulted in one suitable event on July 16, 2008, when two of the THEMIS spacecraft (THEMIS-B and THEMIS-C) encountered the foreshock region during which time the IMF vector $\mathbf{B} = [4.8, -1.6, -0.2]$ nT, corresponding to an IMF cone angle of 19°. This IMF direction is almost antiparallel to the Vlasiator case. Table 1 shows a comparison between the solar wind and IMF parameters for the Vlasiator run and the THEMIS event. We used lagged L1 data (which was validated by comparison with THEMIS) from the OMNI database. Figure 1a shows the THEMIS positions in the Vlasiator modeling of the foreshock using the geocentric interplanetary medium (GIPM) coordinate system [*Bieber and Stone*, 1979], which rotates about the Sun-Earth line such that the IMF is entirely in the second and fourth quadrants of XY plane. This makes the GIPM $Z = 0$ direction comparable to the simulation. In the THEMIS interval the z component of the IMF is small, and hence there is little difference between GSE and GIPM.

Figure 8 shows THEMIS B and THEMIS C Fluxgate Magnetometer [*Auster et al.*, 2008] and combined Electrostatic Analyser and Solid State Telescope [*McFadden et al.*, 2008] data in panels a-d) and e-h), respectively, on July 16, 2008. In THEMIS B, there is a noticeable slope in B_z and B_y, and there are no suprathermal ions or upstream waves before about 23:04 UT. At 23:04 UT, the ions with energies up to 4 or 5 keV are reflected field-aligned ion beams (distributions not shown). This indicates that the spacecraft was outside the foreshock in the beginning of the plotted period. After this, a correlated compression in magnetic field and density follows as higher energy ions are observed, followed by ULF upstream waves. The transient signature is likely due to the motion of the foreshock compressional boundary (e.g. *Sibeck et al.* [2008]) in response to slight IMF changes. Therefore, consistent with Fig. 1a, THEMIS spacecraft are near the foreshock boundary during the event.

Throughout the plotted period, both THEMIS B and C show fluctuations in the magnetic field B_z and B_y components, while the fluctuations in B_x are smaller. The density fluctuates in concert with the magnetic field are indicative of compressive waves, and as the fluctuations are accompanied by suprathermal ions, we conclude that the spacecraft are in the ULF foreshock and observe upstream ULF waves [*Le and Russell*, 1994]. At THEMIS C, which is close to the bow shock surface, the fluctuations are larger both in the magnetic field as well as in density, signifying wave growth towards the bow shock.

Figure 9 shows the Vlasiator data at THEMIS B and THEMIS C as defined in Fig. 1. The simulation time is the same as physical time. Panels 9a and 9c are the magnetic field components and intensity, while panels 9b and 9d are the plasma density. The color-coding and the axis limitations are the same as in Fig. 8 to facilitate comparison to spacecraft observations. At THEMIS B positioned upstream of THEMIS C, the fluctuations are similar in magnitude as in observations, while at THEMIS C position the Vlasiator modeling does not show a similar compression. Looking at Fig. 6a, the duskside cut through the foreshock shows that the wave amplitudes are large near the bow shock, then decrease somewhat, but are largest around 30-40 R_E distance. Note that as THEMIS B is further upstream compared to THEMIS C, the Vlasiator foreshock starts to develop later in the simulation, while at the THEMIS C position the ULF fluctuations start sooner.

Table 2 gives a summary of the detailed comparison between THEMIS and Vlasiator. According to the *Takahashi et al.* [1984] formula, the frequency of upstream ULF waves in the subsolar foreshock should be 0.035 Hz during the THEMIS event, corresponding to a period of 29 s. This is in good agreement with the THEMIS data. For the simulated case, the *Takahashi et al.* [1984] formula predicts a period of 27 s using the run cone angle and IMF strength, again corresponding well with the simulation values. To compute θ_{kB}, the observations were subdivided into 2-minute intervals (50% overlap) and minimum variance analysis was applied to each interval having 3-second smoothed time series. The smoothing was done to remove higher frequency whistler waves known to exist in the foreshock alongside the 30-second waves [*Hoppe et al.*, 1981], so that the θ_{kB} corresponds to the 30-second waves. In the used version of Vlasiator such higher frequency waves are not present, and hence the simulation data did not have to be smoothed. The average θ_{kB} is given as the angle between the average (over the components) minimum variance direction and the IMF, whereas the error indicates the directional spread around this average direction. The approach is similar to that used by *Eastwood et al.* [2004, 2005b]. While the average θ_{kB} are slightly larger in Vlasiator than in the observations, there is a systematic decrease in θ_{kB} further downstream. Furthermore, in the plane defined by the magnetic field and solar wind velocity, the **k** deflection systematically points towards the foreshock edge at THB to being more field-aligned at THC. This is common to both the observations and Vlasiator. The large spread in the observations is in part due to some poor eigenvalue ratios leading to a larger error in minimum variance analysis.

Figure 10 shows examples of the distribution function observed by THEMIS C observations of the ion velocity distribution function (panels a and b), accompanied by a Vlasiator distribution function (panels c and d) at THEMIS C location. All data are given in the coordinates parallel and perpendicular to the magnetic field. The times at which the distributions are taken are marked in Fig. 8 by white horizontal bars in panel 8h. Panels 10a and 10b respectively are taken outside and during the enhancements in the suprathermal ion energy flux visible in Figure 8h, i.e. times when the colorscale is more orange at energies 3000-10,000 eV. The enhancements have the same periodicity as the ULF waves. The Vlasiator distributions (panels 10c-d) are taken at the THC position in the GIPM frame at time t = 500 s and t = 685 s, respectively. The THEMIS C distribution functions show that the suprathermal distributions are more field-aligned or intermediate outside the enhancements (Figure 10a) and hotter and more diffuse-like during the enhancements (Figure 10b). Therefore, the upstream ULF waves may modulate the beam and the shock thereby changing the ion distributions as reported by *Mazelle et al.* [2003] and *Meziane et al.* [2001, 2004]. Vlasiator distributions taken from the THC position and displayed in Fig 10 first show a relatively hot field aligned / intermediate beam (Fig. 10c), while later the distribution is more diffuse (Fig. 10d), in accordance with THEMIS C observations. This indicates a temporal dependency within the same location, while the spatial dependency of the Vlasiator distribution function is addressed more in *Kempf et al.* [2015].

5. Discussion

In this paper we have presented the first detailed modeling results of the ULF foreshock wave field under radial IMF conditions using the new Vlasiator simulation, and compared them to a representative case from THEMIS data records as well as to long known properties of ULF waves from previous studies. The ULF wave periods, propagation angles, polarization and wavelengths both in the parallel and perpendicular direction are in accordance with previous literature [*Le and Russell*, 1994; *Eastwood et al.*, 2005a, b; *Archer et al.*, 2005]. Note that a typical spacecraft apogee is about 20 R_E indicating that the main observational statistical results concern wave properties relatively close to the bow shock, while our analysis concerns the entire foreshock. The comparison with THEMIS data shows that Vlasiator results at the spacecraft locations are in quantitative agreement with the observations. The THEMIS data show that the distribution functions are modulated with the waves, which has been attributed to wave modulation of the shock properties. This is also seen when scrutinising the Vlasiator distribution functions, in line with earlier observations [*Meziane et al.*, 2001, 2004]. We therefore conclude that the Vlasiator ULF foreshock reproduces the ULF foreshock characteristics such that the modeling results can be used to make physical conclusions based on the simulation.

Even though we present modeling results during stationary solar wind conditions, there is considerable variability in the wave characteristics throughout the foreshock. The wave characteristics are in agreement with previous statistics [*Eastwood et al.*, 2005a, b] that are measured during a variety of solar wind conditions, indicating that the foreshock physics is not only driven by external solar wind conditions, but is also influenced by the intrinsic properties of the foreshock. The wave characteristics show generally more variability near the bow shock, and are more coherent further upstream. This is probably due to the more turbulent conditions near the bow shock, where the waves evolve non-linearly as they advect, and where the shock rippling also affects the wave field characteristics. There is also a considerable variability in the Y direction through the foreshock, which we discuss shortly.

To investigate the oblique propagation, we show in Figure 11 first as a dashed black line the Alfvénic dispersion relation of low frequency waves approximated by $\omega = k_{\|} v_A$, and second as solid lines the dispersion relation of the right-handed elliptically polarized waves for a plasma consisting of a solar wind core and a reflected ion beam population. The latter dispersion relation has been obtained using the WHAMP code [e.g., *Kempf et al.*, 2013] with parameters representative of the Vlasiator foreshock in the radial run presented in this paper. Only the dispersion relation where the growth rate is larger than 0.02 is shown. To illustrate the dependence of the dispersion relation on the beam properties, we vary the beam density and beam velocity. The black curve represents a plasma with beam density n_B of 0.5% of the solar wind density, and beam velocity v_B of 1200 km/s. The red curve is with the same beam velocity with a smaller beam density, while the blue curve is with the same beam density with a smaller beam velocity relative to the black curve. As can be seen in Fig. 11, the dispersion relation differs qualitatively from the standard Alfvénic dispersion relation. To the lowest order, the dispersion relation is of the form

$$\omega = -a(n_B)\Omega_p + b(n_B)v_B k_{\|} \quad (1)$$

where a and b are positive dimensionless constants depending on the beam density n_B, Ω_p is the proton cyclotron frequency, v_B is the beam speed and $k_{\|}$ is the wave number parallel to the magnetic field.

As the dispersion relation shows, the wave number k depends on the beam speed and the beam density. Therefore we present the density and the velocity of the backstreaming population relative to the solar wind core population in Figure 12 for three different times. The white arrows identify an individual wave front, illustrated with B_z contours. To separate the solar wind core population from the backstreaming one, all velocity space within a sphere of radius ∼690 km/s centered on the upstream solar wind velocity is considered to be the solar wind population, while the remaining population is considered backstreaming. Moments such as the density or velocity are then computed separately for each population. The method used to separate the core from the backstreaming part of the velocity distribution is correct as long as the backstreaming components have velocities higher than the set separation radius. This is the case in large areas of the foreshock within several R_E of the foreshock edge where fast field-aligned beam populations are seen [*Kempf et al.*, 2015]. Deeper in the foreshock, wave-particle interactions perturb more strongly the backstreaming populations. In such cases, parts of the backstreaming population can be within the separation. Nevertheless in the areas of interest to the following analysis the error thus introduced is within 10%, which does not affect the results presented.

Figures 12a and 12b show that the wave front is born upstream roughly perpendicular to the magnetic field. As the wave advects with the solar wind flow towards the bow shock (Fig. 12c-f) different parts of it encounter plasma with a slower and more dilute beam, making the front oblique close to the foreshock edge. Figure 12c and 12d show that the part of the wave front closest to the foreshock edge, where the beam density and velocity are larger than in the central foreshock, is bent, while the wave front in the central foreshock is less bent. Figure 12e and 12f show that as the wave front gets closer to the bow shock, it is extended through a variety of beam densities and velocities, making the wave front more oblique also in the central part of the foreshock.

According to the dispersion relation of the wave, different parts of the wave front will have a different k. This suggests that refraction may play a role in the bending of the wave fronts also in the radial case that has previously been thought of as a special case where the *Hada et al.* [1987] refraction mechanism has not been thought to operate. Indeed, the

Hada et al. [1987] mechanism concerns larger cone angles, where the spatial variation of the beam population is caused both by the variation in reflection from the bow shock, and the $\mathbf{E} \times \mathbf{B}$ drift that leads to variations in the beam structure. In this paper, the influence of the $\mathbf{E} \times \mathbf{B}$ drift is small, and the variation in the beam density and velocity is caused by the large-scale structure of the foreshock, where in general the highest beam densities and velocities are found at the edges of the foreshock and near the bow shock surface. The quantitative analysis of the beam plasma dispersion relation and its effects on wave refraction in the foreshock will be the subject of a forthcoming study, however, here we can conclude that the wave oblique propagation is due to the variability in the beam density and velocity affecting the refractive index. The highest beam velocities near the foreshock edges are due to a better reflection angle (θ_{Bn}) and the fact that there the reflected particles can propagate more easily without being scattered by the ULF waves, while in the central foreshock the beam particles are subjected to wave-particle interactions that modify the beam properties and decelerate the beam particles.

A clear change in the wave propagation angles appears at backbones or spines originating from the bow shock approximately at $Y = -12$ and 2 R_E (see Fig. 1), although their places vary in the run. Similar spines are observed in our other runs and also with coarser resolution (not shown). They are most prominent in the radial geometry, but can be identified also with other IMF orientations, and hence we interpret that they are physical and not of numerical origin. Although such spines have not been reported before explicitly, in Figure 1 of *Blanco-Cano et al.* [2009], global wave break points are visible such that foreshock edge waves have a different propagation angle compared to the central foreshock. These wave break points are quite subtle, which might be a consequence of the number of particles in the simulation of *Blanco-Cano et al.* [2009]. The Vlasov method, due to its continuous and uniform representation of phase space by construction, is somewhat more advantageous in modeling beam-driven wave instabilities, and in resolving velocity distributions with both low-density and high density regions. While similar phase space resolution can be achieved in PIC simulations by e.g. introducing particle splitting, this introduces another variable into evaluating the correctness of PIC simulations, as the ideal number of particles introduced in a splitting event changes according to the physics involved. In the case of *Blanco-Cano et al.* [2009], Maxwellian particles were split to 16 solar wind particles, indicating that the mass ratio of Maxwellian vs backstreaming particles is 1/16. Typically, Vlasiator's ratio is several magnitudes larger. While this kind of rough density estimate does not provide conclusive evidence in comparing the results with *Blanco-Cano et al.* [2009], it does indicate a possible explanation for the discrepancy.

To investigate the nature of the spines we highlight their approximate positions as dashed white lines in Fig. 12. Figure 12 indicates that at the spine location approximately at $Y = 2\ R_E$ at these time instants, there is a sinusoidal-like backstreaming beam with enhanced density moving slowly relative to its surroundings. To investigate the spines in time, we present as a supplementary material a movie showing the velocity of the reflected particles. In this movie, it is evident that two processes are behind the spines. First, there are transient preferential places of reflection at the bow shock, from which denser beams are emitted. Through a denser beam, the refractive index would change considerably, which would make the wave fronts bend. Second, there is a global structure in the foreshock, in which the waves are more easily growing and propagating at the foreshock edges, where the density and velocity of the backstreaming population is higher. In the central foreshock the beams travel slower due to the enhanced scattering by the waves, and due to less efficient reflection (see also *Kempf et al.* [2015]). Therefore, there is a global variability in the wave propagation between the edges and the central foreshock, leading to a wave interference approximately at the spine location. This kind of global structure in the foreshock wave field has naturally not been observed, since it would require multiple spacecraft around the foreshock, and fortuitous solar wind conditions.

The large-scale structure of the foreshock beam density and velocity also determines the variability of the wave period within the foreshock. The dispersion relation in Eq. 1 indicates that the wave period and wavelength should be inversely proportional to the beam velocity. Indeed, by looking at the dusk foreshock in Fig. 12 and the wave period against the distance from the duskside bow shock in Fig. 5 (red dots) we observe that the wave period increases roughly with decreasing beam speed. Similarly, in the vicinity of the bow shock where the beam speed is larger, the wavelength is smaller (Fig. 6), again in line with the dispersion relation.

In conclusion, we find that the variability of the backstreaming beam density and velocity determines the large-scale structure of the foreshock, which affects the wave frequency, wavelength and oblique propagation. For observational studies, we predict that the wave propagation angle should be larger in the vicinity of the foreshock edge and smaller far upstream, and that it would depend heavily on the gradient in the beam density and velocity. Similarly, we predict that the foreshock distribution function shapes should correspond to the spatial variations of the beam density and velocity that may be caused by optimal reflection sites from the bow shock or by global wave interference through the foreshock.

Acknowledgments. Vlasiator (http://vlasiator.fmi.fi) was developed with the European Research Council Starting grant (200141-QuESpace) granted to MP in 2007. The Academy of Finland has also supported the Vlasiator development. We gratefully acknowledge CSC - IT Center for Science for granting us pilot usage of the Sisu supercomputer. VisIt [*Childs et al.*, 2012] is used to visualise Vlasiator data. The work at FMI is supported by the Academy of Finland grant numbers 138599 and 267144. Work at ICL is supported by STFC grant number ST/K001051/1. UG is supported by the German Research Foundation (DFG) grant GA 1968/1. Vlasiator data policy is described in http://vlasiator.fmi.fi/rules.php, THEMIS observations and software are fully accessible to the research community (see http://themis.igpp.ucla.edu).

References

von Alfthan, S., D. Pokhotelov, Y. Kempf, S. Hoilijoki, I. Honkonen, A. Sandroos, and M. Palmroth, (2014),Vlasiator: First global hybrid-Vlasov simulations of Earth's foreshock and magnetosheath, *J. Atmos. Solar Terr. Phys.*, 120, 24-35, doi:10.1016/j.jastp.2014.08.012

Angelopoulos, V., The THEMIS Mission (2008), *Space Sci. Rev.*, 141, pp 5-34, doi:10.1007/s11214-008-9336-1

Archer, M., T. S. Horbury, E. A. Lucek, C. Mazelle, A. Balogh, and I. Dandouras (2005), Size and shape of ULF waves in the terrestrial foreshock, *J. Geophys. Res.*, 110, A05208, doi:10.1029/2004JA010791.

Auster, H. U. et al., The THEMIS Fluxgate Magnetometer (2008), *Space Sci. Rev.*, pp 235-264, doi:10.1007/s11214-008-9365-9

Bieber, J. W. and Stone, E. C., Energetic electron bursts in the magnetopause electron layer and in interplanetary space, in: *Proceedings of Magnetospheric Boundary Layers Conference*, ESA SP-148, 131-135, 1979.

Blanco-Cano, X., N. Omidi, and C. T. Russell (2006), Macrostructure of collisionless bow shocks: 2. ULF waves in the foreshock and magnetosheath, J. Geophys. Res., 111, A10205, doi:10.1029/2005JA011421.

Blanco-Cano, X., N. Omidi, and C. T. Russell (2009), Global hybrid simulations: Foreshock waves and cavitons under radial interplanetary magnetic field geometry, J. Geophys. Res., 114, A01216, doi:10.1029/2008JA013406.

Blanco-Cano, X., P. Kajdič, N. Omidi, and C. T. Russell (2011), Foreshock cavitons for different interplanetary magnetic field geometries: Simulations and observations, *J. Geophys. Res.*, 116, A09101, doi:10.1029/2010JA016413.

Childs, H., E. Brugger, B. Whitlock, J. Meredith, S. Ahern, D. Pugmire, K. Biagas, M. Miller, C. Harrison, G. H. Weber, H. Krishnan, T. Fogal, A. Sanderson, C. Garth, E. Wes Bethel, D. Camp, O. Rübel, M. Durant, J. M. Favre, P. Navrátil, (2012) VisIt: An End-User Tool For Visualizing and Analyzing Very Large Data, *High Performance Visualization–Enabling Extreme-Scale Scientific Insight*, 357-372

Eastwood, J. P., A. Balogh, M. W. Dunlop, T. S. Horbury, and I. Dandouras (2002) Cluster observations of fast magnetosonic waves in the terrestrial foreshock, *Geophys. Res. Lett.*, 29(22), 2046, doi:10.1029/2002GL015582

Eastwood, J. P., A. Balogh, C. Mazelle, I. Dandouras, and H. Rème (2004), Oblique propagation of 30 s period fast magnetosonic foreshock waves: A Cluster case study, *Geophys. Res. Lett.*, 31, L04804, doi:10.1029/2003GL018897.

Eastwood, J. P., A. Balogh, E. A. Lucek, C. Mazelle, and I. Dandouras (2005), Quasi-monochromatic ULF foreshock waves as observed by the four-spacecraft Cluster mission: 1. Statistical properties, *J. Geophys. Res.*, 110, A11219, doi:10.1029/2004JA010617.

Eastwood, J. P., A. Balogh, E. A. Lucek, C. Mazelle, and I. Dandouras (2005), Quasi-monochromatic ULF foreshock waves as observed by the four-spacecraft Cluster mission: 2. Oblique propagation, *J. Geophys. Res.*, 110, A11220, doi:10.1029/2004JA010618.

Fairfield, D. H. (1969), Bow shock associated waves observed in the far upstream interplanetary medium, *J. Geophys. Res.*, 74(14), 3541-3553, doi:10.1029/JA074i014p03541.

Fuselier, S. A., M. F. Thomsen, J. T. Gosling, S. J. Bame, and C. T. Russell (1986), Gyrating and intermediate ion distributions upstream from the Earth's bow shock, *J. Geophys. Res.*, 91(A1), 91-99, doi:10.1029/JA091iA01p00091.

Gary, S. P. (1993) Theory of Space Plasma Microinstabilities, Cambridge University Press, New York

Greenstadt, E. W., I. M. Green, G. T. Inouye, A. J. Hundhausen, S. J. Bame, and I. B. Strong (1968), Correlated magnetic field and plasma observations of the Earth's bow shock, *J. Geophys. Res.*, 73(1), 51-60, doi:10.1029/JA073i001p00051.

Greenstadt, E. W., G. Le, and R. J. Strangeway (1995), ULF waves in the foreshock, *Adv. Space Res.*, 15, 71-84.

Hada, T., C. F. Kennel, and T. Terasawa (1987), Excitation of compressional waves and the formation of shocklets in the Earth's foreshock, *J. Geophys. Res.*, 92(A5), 4423-4435, doi:10.1029/JA092iA05p04423.

Hoppe, M. M., and C. T. Russell (1983) Plasma rest frame frequencies and polarizations of the low-frequency upstream waves: ISEE 1 and 2 observations, *J. Geophys. Res.*, 88, 2021-2028.

Hoppe, M. M., C. T. Russell, L. A. Frank, T. E. Eastman, and E. W. Greenstadt (1981) Upstream hydromagnetic waves and their association with backstreaming ion populations - ISEE 1 and 2 observations, *J. Geophys. Res.*, 86, 44714492, doi: 10.1029/JA086iA06p04471.

Hsieh, W.-C., and J.-H. Shue (2013), Dependence of the oblique propagation of ULF foreshock waves on solar wind parameters, *J. Geophys. Res.*, 118, 4151-4160, doi:10.1002/jgra.50225.

Janhunen, P., M. Palmroth, T. V. Laitinen, I. Honkonen, L. Juusola, G. Facskó, and T. I. Pulkkinen (2012), The GUMICS-4 global MHD magnetosphere - ionosphere coupling simulation, *J. Atm. Solar Terr. Phys.*, 80, 48-59, doi:10.1016/j.jastp.2012.03.006

Karimabadi, H., V. Roytershteyn, H. X. Vu, Y. A. Omelchenko, J. Scudder, W. Daughton, A. Dimmock, K. Nykyri, M. Wan, D. Sibeck, M. Tatineni, A. Majumdar, B. Loring, and B. Geveci, (2014) The link between shocks, turbulence, and magnetic reconnection in collisionless plasmas, *Phys. Plasmas*, 21, 062308, doi: 10.1063/1.4882875

Kempf, Y., D. Pokhotelov, S. von Alfthan, A. Vaivads, M. Palmroth, and H. E. J. Koskinen (2013) Wave dispersion in the hybrid-Vlasov model: Verification of Vlasiator, *Phys. Plasmas*, 20, doi:10.1063/1.4835315

Kempf, Y., D. Pokhotelov, O. Gutynska, L. B. Wilson III, B. M. Walsh, S. von Alfthan, O. Hannuksela, D. G. Sibeck, and M. Palmroth (2015) Ion distributions in the Earth's foreshock: hybrid-Vlasov simulation and THEMIS observations, *J. Geophys. Res.*, 120, doi:10.1002/2014JA020519

Killen, K., N. Omidi, D. Krauss-Varban, and H. Karimabadi (1995) Linear and nonlinear properties of ULF waves driven by ring-beam distribution functions, *J. Geophys. Res.*, 100, 5835-5852, doi:10.1029/94JA02899

Le, G., and C. T. Russell (1994) The Morphology of ULF Waves in the Earth's Foreshock, in Solar Wind Sources of Magnetospheric Ultra-Low-Frequency Waves, edited by M. J. Engebretson, K. Takahashi, and M. Scholer, *Geophysical Monograph 81*, p.81-98, AGU, Washington DC, 1994.

Mazelle, C., et al. (2003) Production of gyrating ions from nonlinear wave-particle interaction upstream from the Earth's bow shock: A case study from Cluster-CIS, *Planel Space Sci.*, 51, 785-795.

McFadden, J. P., Carlson, C. W., Larson, D., Angelopoulos, V., Ludlam, M., Abiad, R., Elliott, B., Turin, P., Marckwordt, M. (2008), The THEMIS ESA plasma instrument and in-flight calibration, *Space Sci. Rev.*, doi: 10.1007/s11214-008-9440-2.

Meziane, K., C. Mazelle, R. P. Lin, D. LeQuéau, D. E. Larson, G. K. Parks, and R. P. Lepping (2001), Three-dimensional observations of gyrating ion distributions far upstream from the Earth's bow shock and their association with low-frequency waves, *J. Geophys. Res.*, 106(A4), 5731-5742, doi:10.1029/2000JA900079.

Meziane, K., C. Mazelle, M. Wilber, D. LeQuéau, J. P. Eastwood, H. Réme, I. Dandouras, J. A. Sauvaud, J. M. Bosqued, G. K. Parks, L. M. Kistler, M. McCarthy, B. Klecker, A. Korth, M. B. Bavassano-Cattaneo, R. Lundin, and A. Balogh, A. (2004) Bow shock specularly reflected ions in the presence of low-frequency electromagnetic waves: a case study, *Ann. Geophys.*, 22, 2325-2335, doi:10.5194/angeo-22-2325-2004.

Omidi, N., X. H. Karimabadi, D. Krauss-Varban, and K. Killen (1994) Generation and nonlinear evolution of oblique magnetosonic waves: Application to foreshock and comets, in *Solar System Plasma Physics: Resolution of Processes in Space and Time, Geophys. Monogr. Ser.*, vol. 84, edited by J. L. Burch, pp. 71-84, AGU, Washington, D. C.

Omidi, N., X. Blanco-Cano, and C. T. Russell (2005), Macrostructure of collisionless bow shocks: 1. Scale lengths, *J. Geophys. Res.*, 110, A12212, doi:10.1029/2005JA011169.

Omidi, N., D. G. Sibeck, and X. Blanco-Cano (2009), Foreshock compressional boundary, *J. Geophys. Res.*, 114, A08205, doi:10.1029/2008JA013950.

Paschmann, G., N. Sckopke, N., J. R. Asbridge, S. J. Bame, J. T. Gosling (1980) Energization of solar wind ions by reflection from the earth's bow shock, *J. Geophys. Res.*, 85, 4689-4693

Paschmann, G., N. Sckopke, N., I. Papamastorakis, J. R. Asbridge, S. J. Bame, J. T. Gosling (1981) Characteristics of reflected and diffuse ions upstream from the earth's bow shock, *J. Geophys. Res.*, 86, 4355-4364

Palmroth, M., I. Honkonen, A. Sandroos, Y. Kempf, S. von Alfthan, and D. Pokhotelov, (2013) Preliminary testing of global hybrid-Vlasov simulation: Magnetosheath and cusps under northward interplanetary magnetic field, *J. Atmos. Solar Terr. Phys.*, 99, 41-46, doi:10.1016/j.jastp.2012.09.013

Pokhotelov, D., S. von Alfthan, Y. Kempf, R. Vainio, H. E. J. Koskinen, and M. Palmroth (2013) Ion distributions upstream and downstream of the Earth's bow shock: first results from Vlasiator, *Ann. Geophys.*, 31, 2207-2212, doi:10.5194/angeo-31-2207-2013.

Rojas-Castillo, D., X. Blanco-Cano, P. Kajdič, and N. Omidi (2013), Foreshock compressional boundaries observed by Cluster, *J. Geophys. Res.*, 118, 698-715, doi:10.1029/2011JA017385.

Russell, C. T., and M. M. Hoppe (1983) Upstream waves and particles, *Space Sci. Rev.*, 34, 155-172.

Russell, C T., J. G. Luhmann, R. C. Elphic, D. J. Southwood, M. F. Smith, and A. D. Jonhnstone (1987) Upstream waves simultaneously observed by ISEE and UKS, *J. Geophys. Res.*, 92, 7354-7362

Sibeck, D. G., N. Omidi, I. Dandouras, and E. A. Lucek, (2008) On the edge of the foreshock: model-data comparisons, *Ann. Geophys.*, 26, 1539-1544

Takahashi, K., R. L. McPherron, and T. Terasawa (1984), Dependence of the spectrum of Pc 3-4 pulsations on the interplanetary magnetic field, *J. Geophys. Res.*, 89, 2770-2780

White, L., and A. Adcroft (2008), A high-order finite volume remapping scheme for nonuniform grids: The piecewise quartic method (PQM) *J. Comp. Phys.*, 227, 7394-7422, doi:10.1016/j.jcp.2008.04.026

Winske, D. (1985) Hybrid simulation codes with application to shocks and upstream waves *Space Sci. Rev.*, 42, 53-66.

Winske, D., C. S. Wu, Y. Y. Li, Z. Z. Mou, and S. Y. Guo (1985) Coupling of newborn ions to the solar wind by electromagnetic instabilities and their interaction with the bow shock *J. Geophys. Res.*, 90, 2713-2726.

Zerroukat, M. and Allen, T. (2012), A three-dimensional monotone and conservative semi-Lagrangian scheme (SLICE-3D) for transport problems. *Q.J.R. Meteorol. Soc.*, 138: 1640-1651. doi: 10.1002/qj.1902

Table 1. Solar wind and IMF parameters for the July 16, 2008 THEMIS observations compared to the Vlasiator run.

	IMF [nT]	Cone angle [deg]	Density [cm^{-3}]	Velocity [km/s]
Vlasiator	[-4.9, 0.4, 0]	5	3.3	600
THEMIS	[4.8, -1.6, -0.2,]	19	1.8	666

Table 2. Wave characteristics in THEMIS and Vlasiator, using the GIPM coordinate system. THEMIS data are based on analysis during the period of ULF waves.

	THEMIS B	Vlasiator	THEMIS C	Vlasiator
$[X, Y, Z]_{GIPM}$	[16.2, 9.3, -9.1]	[16.2, 9.3, 0]	[11.3, 9.4, -6.5]	[11.3, 9.4, 0]
Period (B_x)	39 s	29 s	32 s	31 s
Period (B_y)	33 s	26 s	30 s	28 s
Period (B_z)	33 s	26 s	28 s	28 s
Period (B)	39 s	32 s	39 s	31 s
θ_{kB}	20°±36°	24°±18°	10°±39°	15°±14°

Figure 1. a) Color-coding shows Vlasiator's modeling of logarithm of plasma density within the Earth's foreshock at time 500 s from the start of the simulation in SI units, m^{-3}. The black dots indicate the positions of virtual spacecraft, where data for the analysis are taken from. The grey dot indicates the position of the virtual spacecraft for which data are given in Figure 2. The two red dots indicate the positions of THEMIS C (closer to shock surface) and THEMIS B (further from the shock surface), for reference. b) Example of the distribution function at position $[X, Y] = [18, -5]$ R_E (colored with a grey dot) as a cut in the velocity XZ plane, again in SI units, s^3m^{-6}.

Figure 2. Time series of the virtual spacecraft in Fig. 1 from the position $[X, Y] = [18, -5]R_E$. a) Plasma density, b) magnetic field intensity, c)-e) x, y, and z components of the magnetic field, respectively, against time in simulation.

Figure 3. a) Histogram of the wave periods from the virtual spacecraft positions in Fig. 1, evaluated from the Fourier transform of the magnetic field z component. b) Histogram of the wave propagation directions with respect of the ambient IMF (θ_{kB}), evaluated using the virtual spacecraft time series in the minimum variance analysis.

Figure 4. Color-coding shows the simulation B_z component representing an Alfvénic disturbance, while the contours are taken from B_y illustrating the wave fronts. The arrows are the x and y components of the minimum variance directions calculated from the virtual spacecraft magnetic field temporal data. The red, green and blue lines in the dusk, central, and dawn edge of the foreshock, respectively, are used to illustrate where data are taken for the wavelength analysis discussed in Fig. 6.

Figure 5. a) Wave period against virtual spacecraft location on X axis, with those periods based on time series of virtual spacecraft located in the dusk (dawn) side foreshock as red (blue). b) Wave propagation direction with respect to the IMF direction against the virtual spacecraft location on X axis with similar color-coding as in panel a).

Figure 6. a)-c) B_z component taken at the dusk, central and dawn side of the foreshock, respectively, along the distance of red, green, and blue lines illustrated in Fig. 4. Distance is evaluated as $\sqrt{X^2 + Y^2 + Y^2}$ of the line coordinates. The data are taken at lines which are cuts through space at the time instant 500 s, when the foreshock is fully developed. Panel d) shows the wavelength of the B_z components in panels a)-c), using the same color-coding. The wavelength is evaluated as a distance between peak values, and plotted as a function of distance on the line.

Figure 7. Polarization of the foreshock wave field at virtual spacecraft position [18, -5]R_E during $255.5 - 474.5$ s (see Fig. 2), with the IMF direction out of the plane towards the viewer. The open dot marks the start of the data set, indicating that the wave is left-handed in the virtual spacecraft frame of reference.

Figure 8. THEMIS B observations for a) magnetic field components B_x, B_y, B_z in blue, green, and red, respectively, and magnetic field intensity (black), b) density (as measured both form ions, and electrons in red and blue, respectively), c) velocity components v_x, v_y, and v_z in blue, green and red, respectively, and speed (black) and d) ion energy spectrogram with the color indicating differential energy flux. Panels e-h) show the observations from THEMIS C in the same format.

Figure 9. a-b) Vlasiator results at THEMIS B and c-d) THEMIS C spacecraft position. Panels a) and c) are the magnetic field components B_x, B_y, B_z in blue, green, and red, respectively, and magnetic field intensity (black). Panels b) and d) are the density.

Figure 10. a-b) THEMIS C respectively outside and during the enhancements in the suprathermal ion energy flux visible in Figure 8h. Panels c-d) are the Vlasiator distributions taken at the THC position in the GIPM frame at time t = 500 s and t = 685 s, respectively. Note that the IMF in the simulation is antiparallel to the THEMIS data, hence the beams are also antiparallel in this projection, making the distribution function mirrored.

Figure 11. Dispersion relation of parallel propagating right-hand polarized unstable waves in a beam plasma, with varying beam density and velocity, color-coded as indicated in the legend. Displayed also are the Alfvénic dispersion relation and the resonance conditions for the two beam velocities.

Figure 12. Density (left column) and velocity relative to the solar wind core population (right column) of the backstreaming population, for three time instants, 450 s (first row), 510 s (second row), and 570 s (bottom row). Contour lines show B_z at values -0.01 nT (blue) and 0.01 nT (red) illustrating wave fronts. The white arrows identify an individual wave front, being born perpendicular to the magnetic field direction, and later becoming oblique (see text for details).

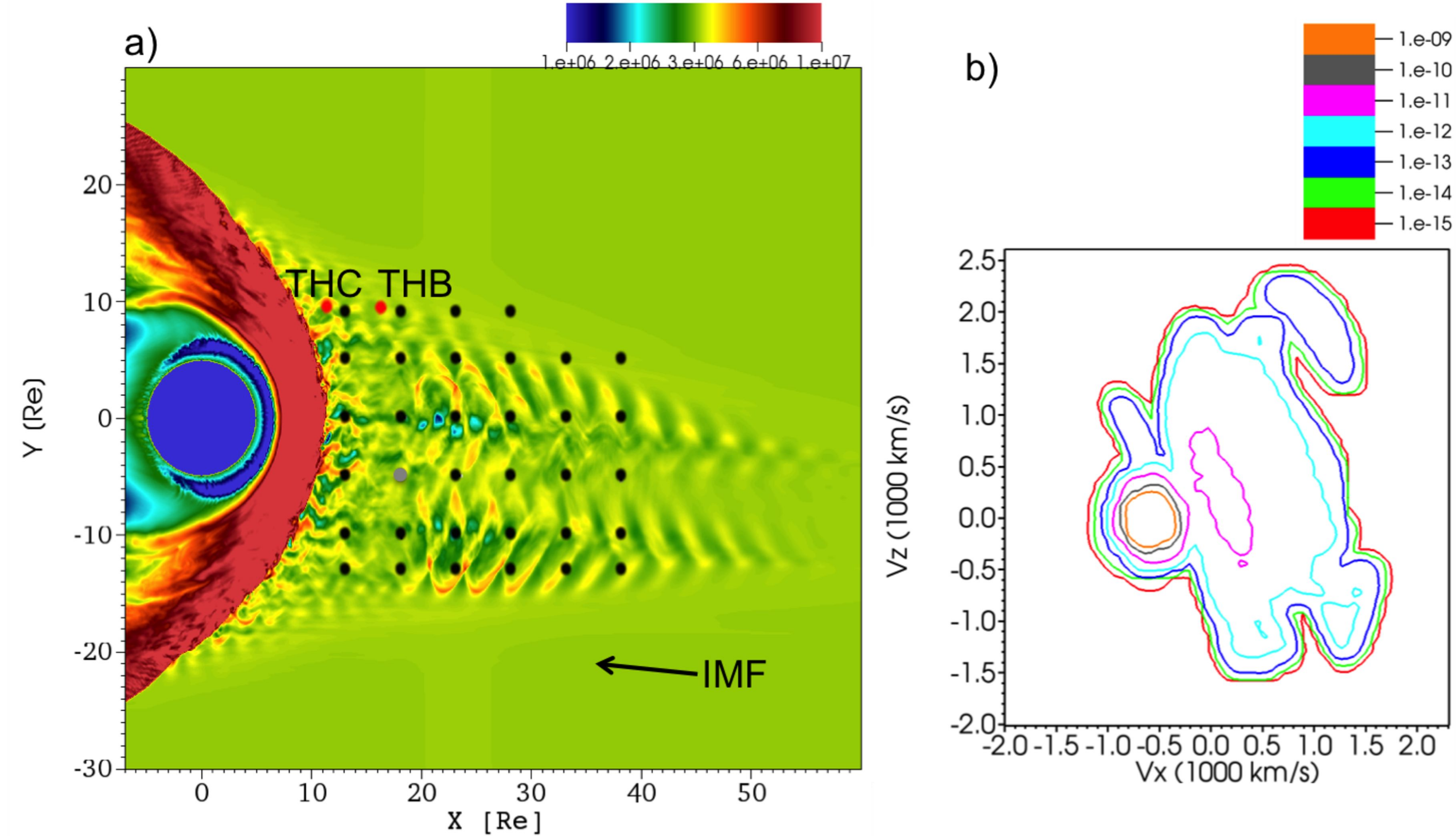
a)
1.e+06 2.e+06 3.e+06 6.e+06 1.e+07
THC THB
IMF
Y (Re)
X [Re]
b)
1.e-09
1.e-10
1.e-11
1.e-12
1.e-13
1.e-14
1.e-15
Vz (1000 km/s)
Vx (1000 km/s)

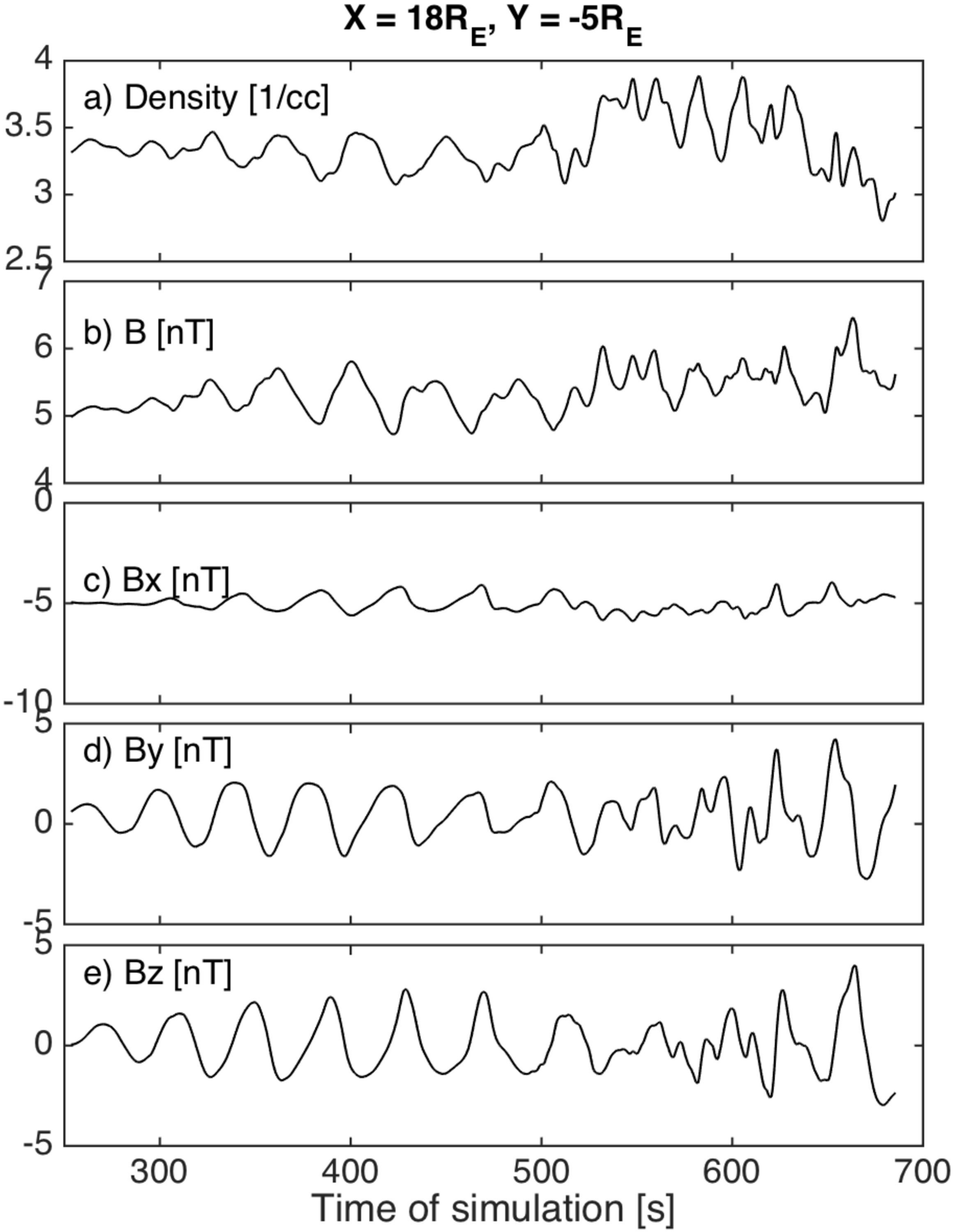
X = 18R_E, Y = -5R_E
a) Density [1/cc]
b) B [nT]
c) Bx [nT]
d) By [nT]
e) Bz [nT]
4
3.5
3
2.5
7
6
5
4
0
-5
-10
5
0
-5
5
0
-5
300
400
500
600
700
Time of simulation [s]

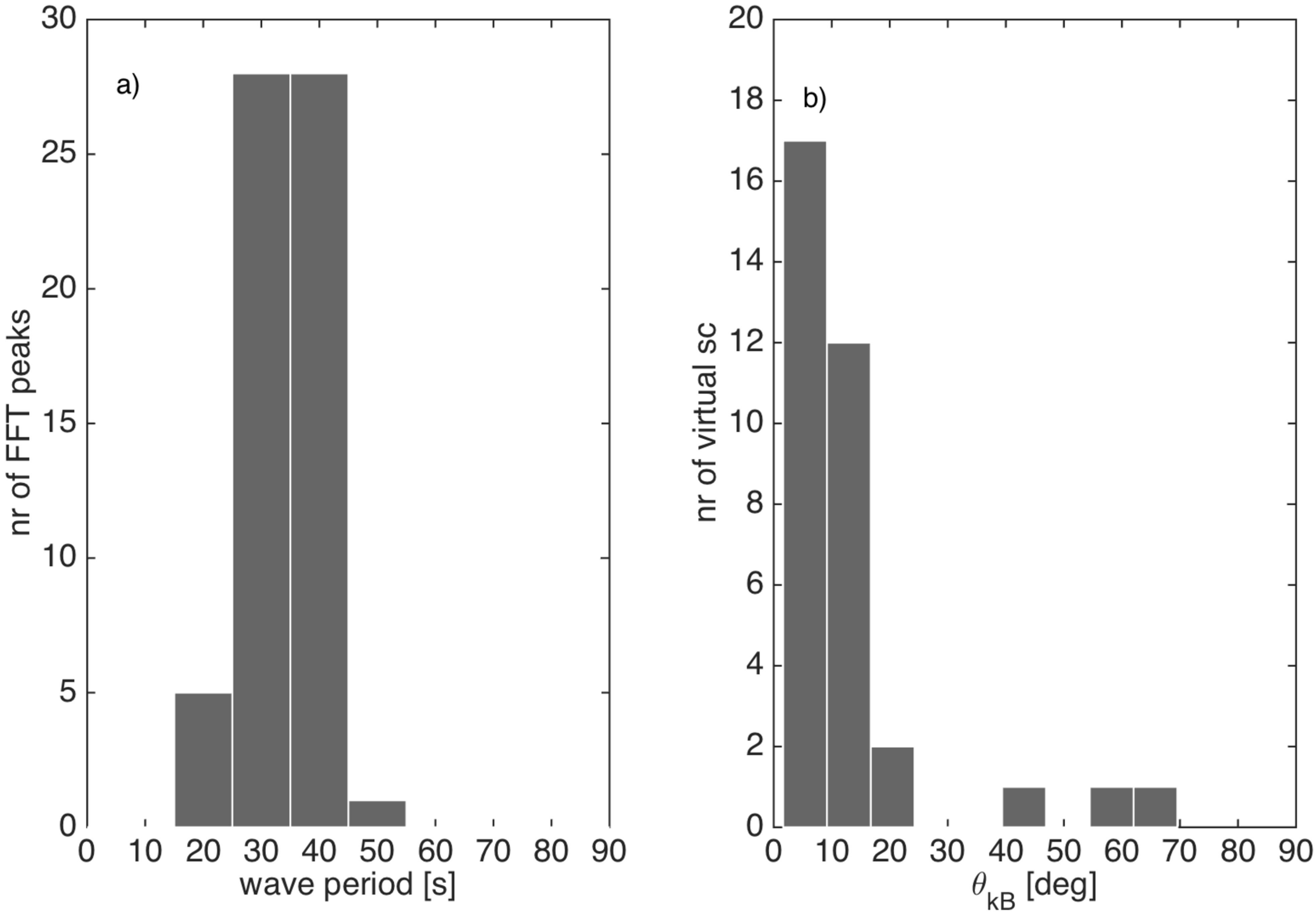

a)
nr of FFT peaks
wave period [s]
0
5
10
15
20
25
30
0
10
20
30
40
50
60
70
80
90
b)
nr of virtual sc
θ_{kB} [deg]
0
2
4
6
8
10
12
14
16
18
20
0
10
20
30
40
50
60
70
80
90

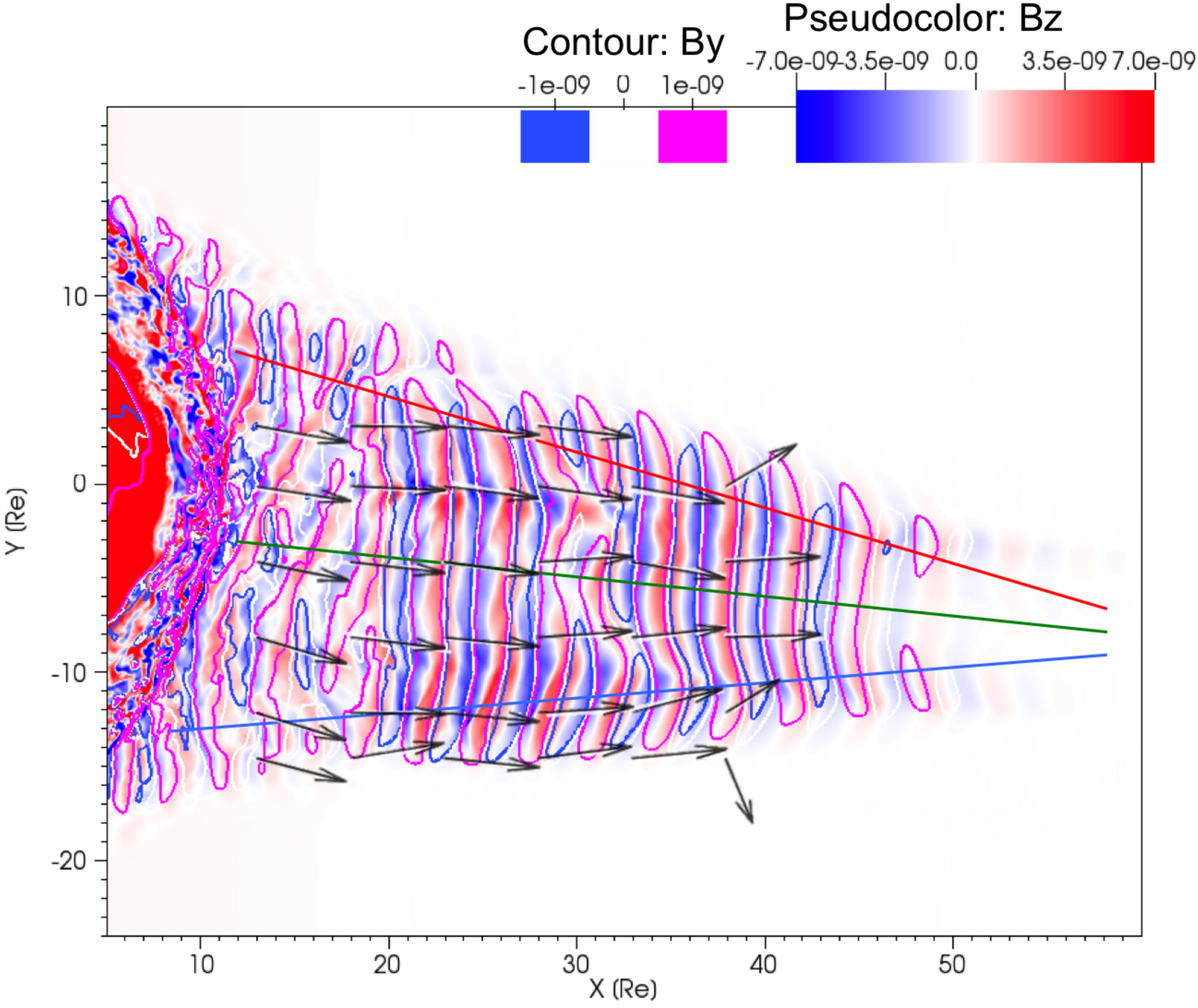
Contour: By
-1e-09
0
1e-09
Pseudocolor: Bz
-7.0e-09
-3.5e-09
0.0
3.5e-09
7.0e-09
10
0
-10
-20
Y (Re)
10
20
30
40
50
X (Re)

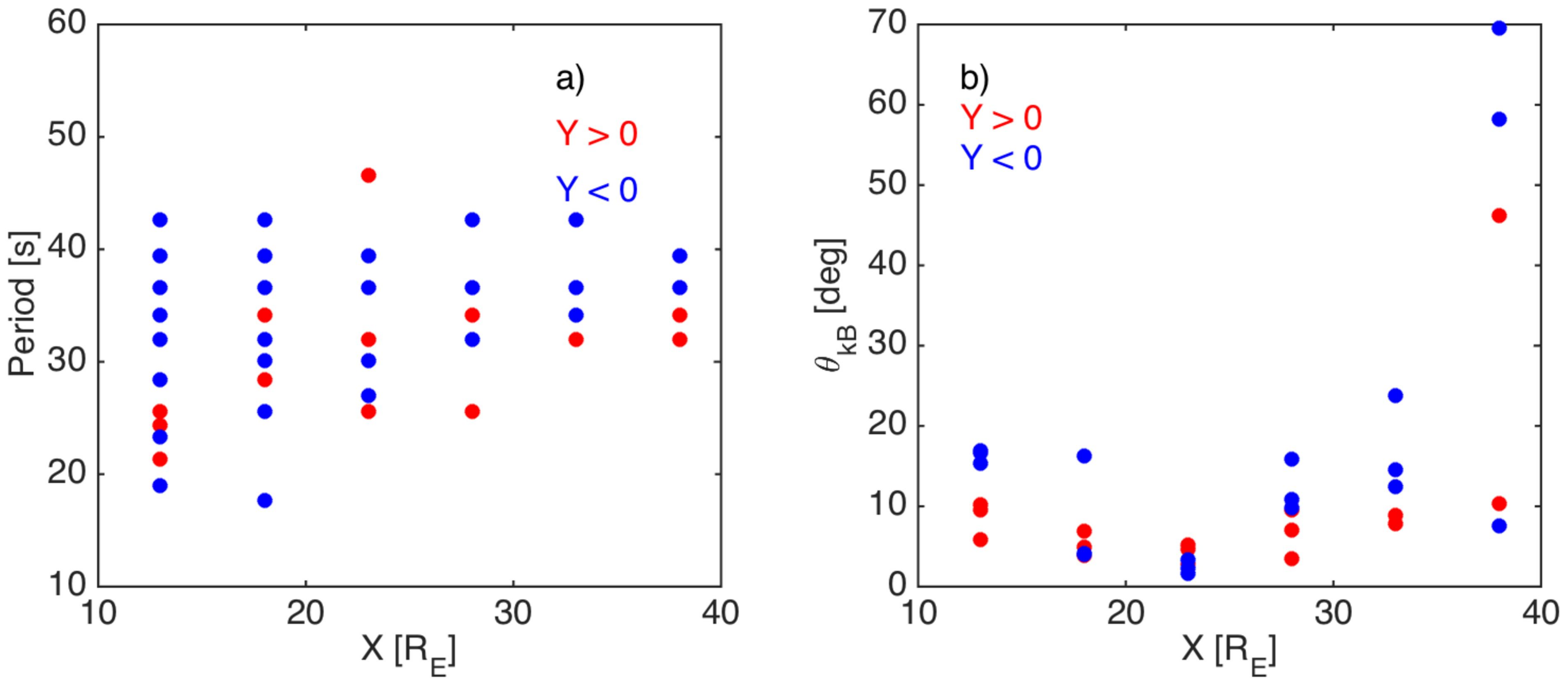
a)
Y > 0
Y < 0
Period [s]
X [R_E]
b)
Y > 0
Y < 0
θ_kB [deg]
X [R_E]

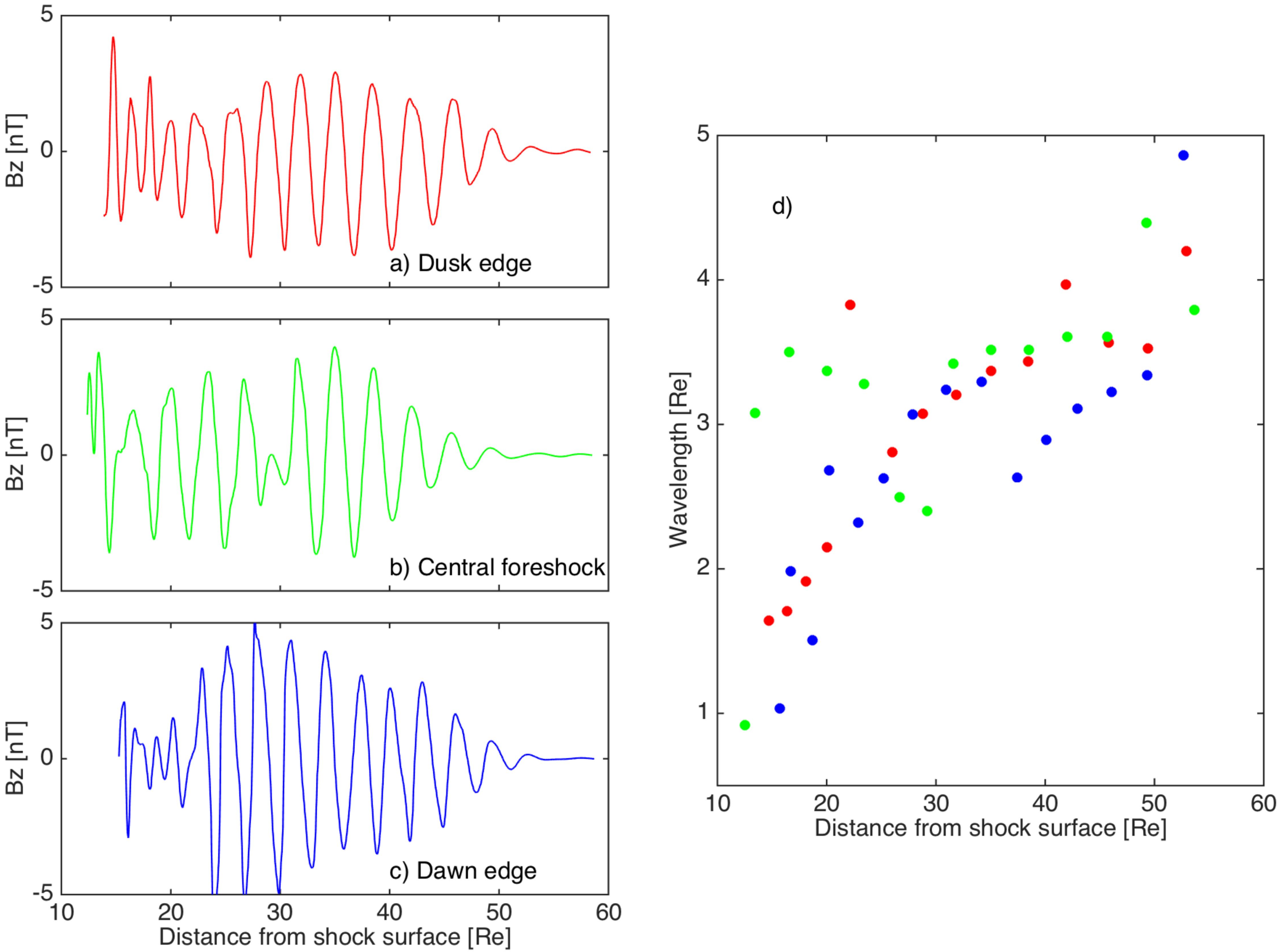

5
0
-5
Bz [nT]
a) Dusk edge
b) Central foreshock
c) Dawn edge
10
20
30
40
50
60
Distance from shock surface [Re]
d)
Wavelength [Re]
1
2
3
4

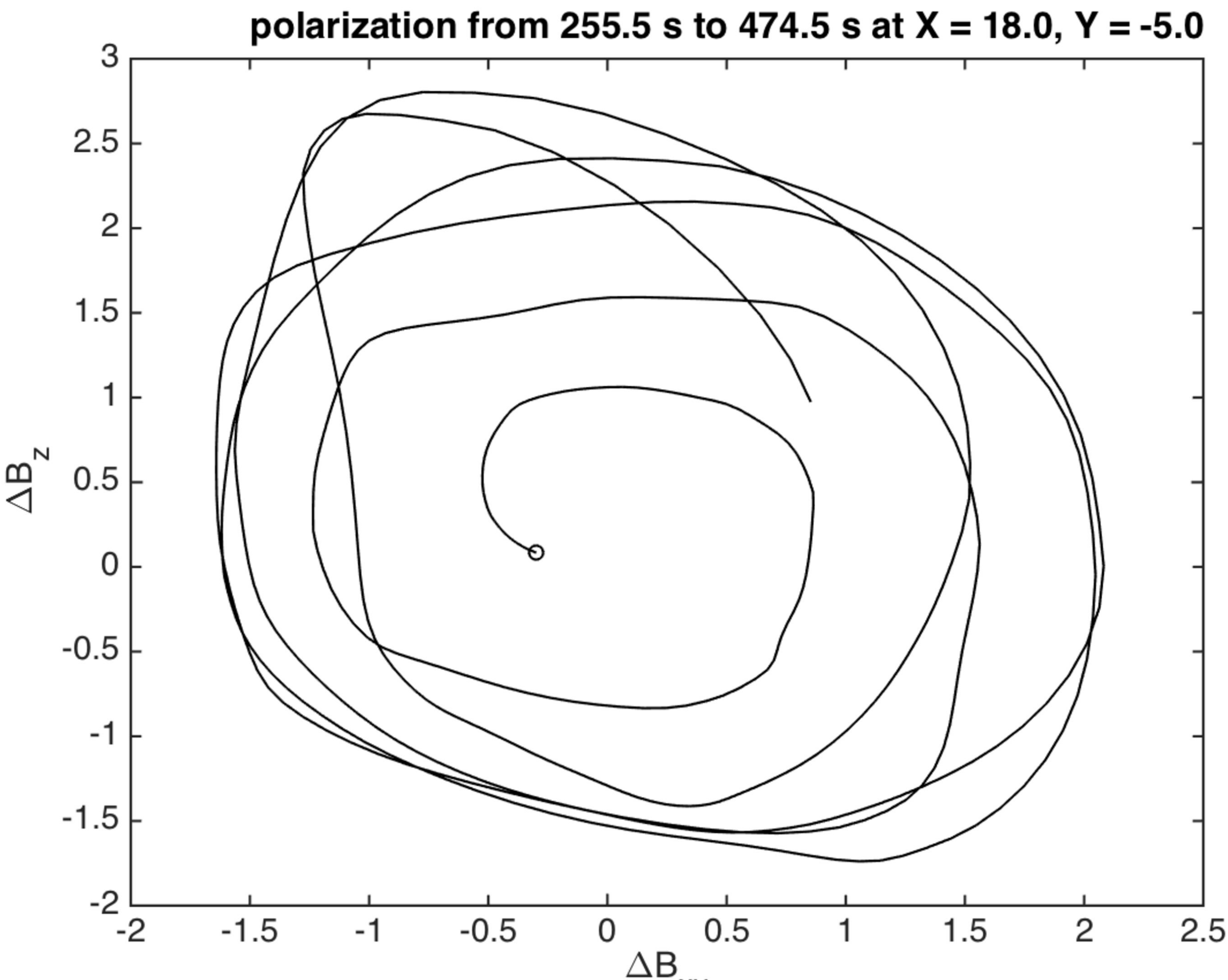
polarization from 255.5 s to 474.5 s at X = 18.0, Y = -5.0
3
2.5
2
1.5
1
0.5
0
-0.5
-1
-1.5
-2
-2
-1.5
-1
-0.5
0
0.5
1
1.5
2
2.5
ΔB_z
ΔB_xy

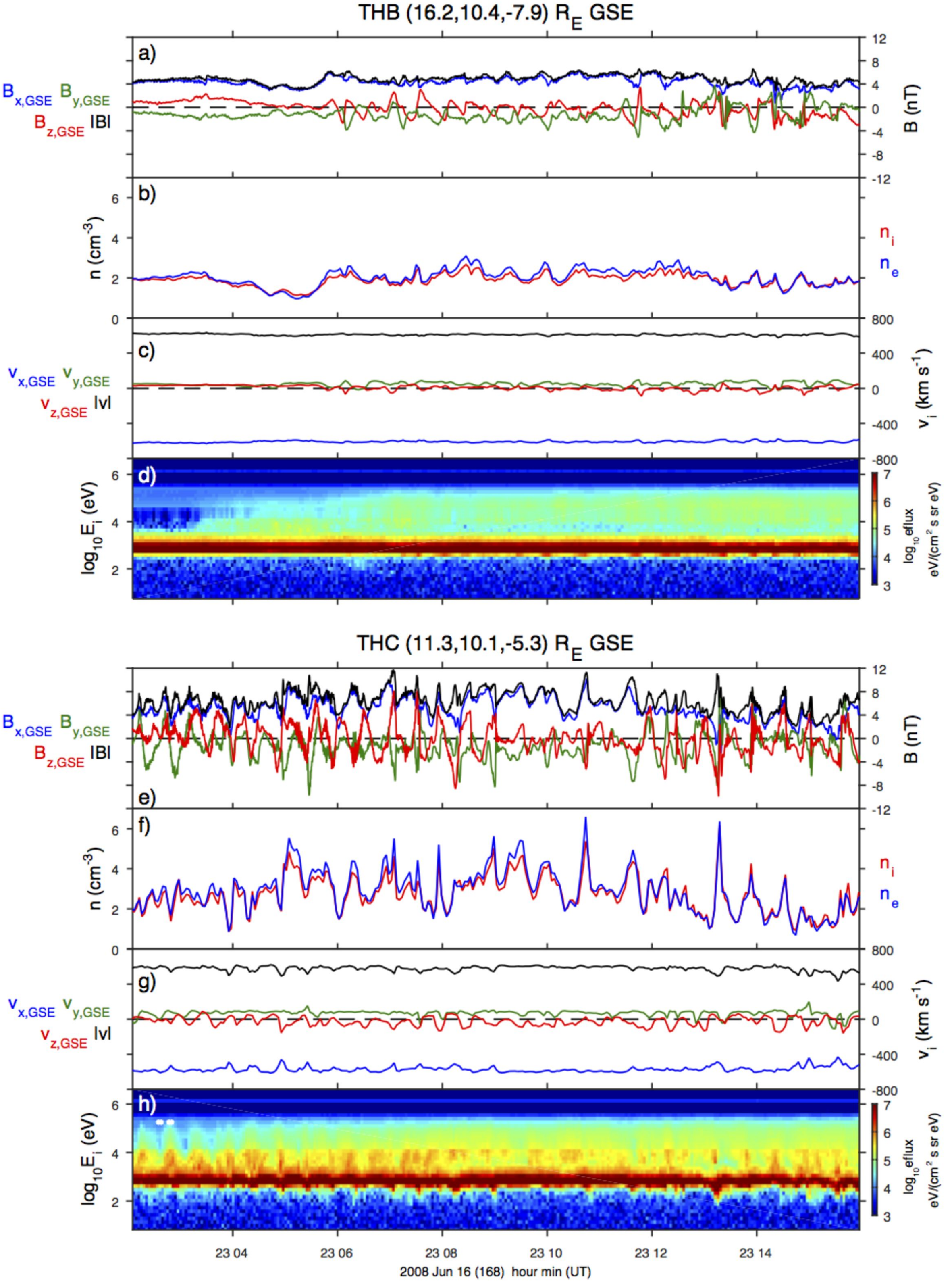

THB (16.2,10.4,-7.9) R_E GSE
a)
B_x,GSE B_y,GSE
B_z,GSE |B|
B (nT)
b)
n (cm^-3)
n_i
n_e
c)
v_x,GSE v_y,GSE
v_z,GSE |v|
v_i (km s^-1)
d)
log10 E_i (eV)
log10 eflux
eV/(cm^2 s sr eV)
THC (11.3,10.1,-5.3) R_E GSE
e)
B_x,GSE B_y,GSE
B_z,GSE |B|
B (nT)
f)
n (cm^-3)
n_i
n_e
g)
v_x,GSE v_y,GSE
v_z,GSE |v|
v_i (km s^-1)
h)
log10 E_i (eV)
log10 eflux
eV/(cm^2 s sr eV)
23 04
23 06
23 08
23 10
23 12
23 14
2008 Jun 16 (168) hour min (UT)

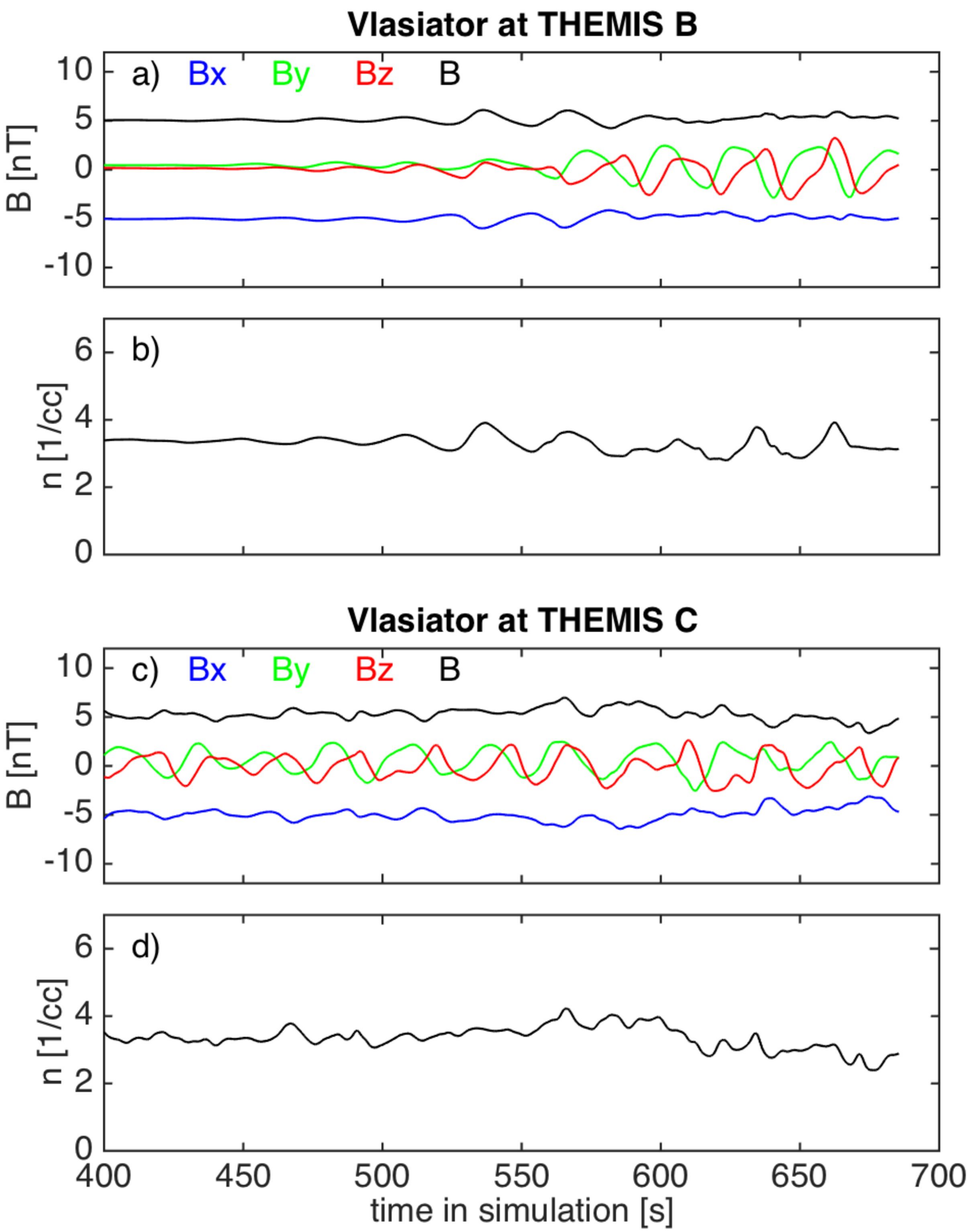

Vlasiator at THEMIS B
a) Bx By Bz B
B [nT]
b)
n [1/cc]
Vlasiator at THEMIS C
c) Bx By Bz B
B [nT]
d)
n [1/cc]
400 450 500 550 600 650 700
time in simulation [s]

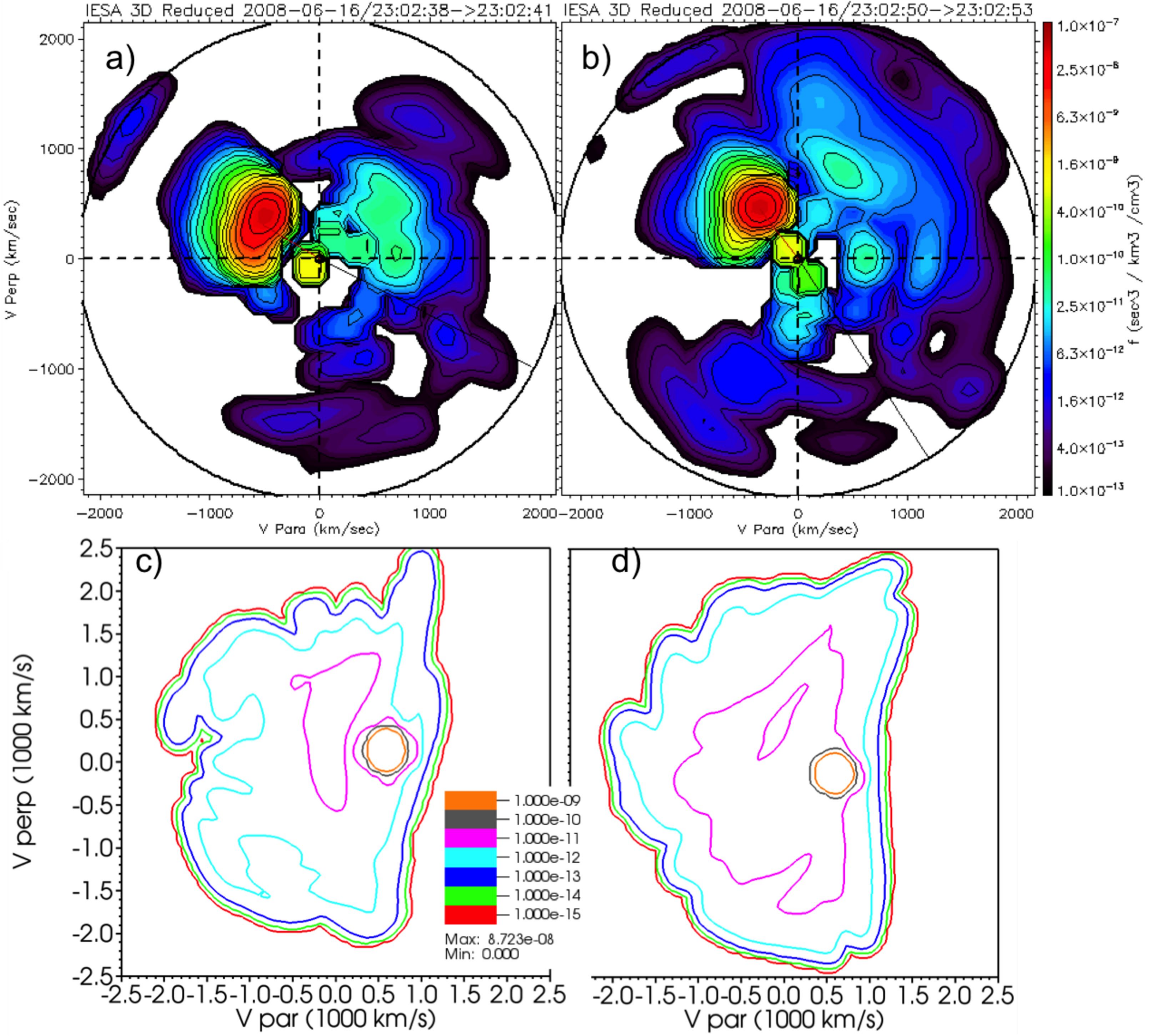

IESA 3D Reduced 2008-06-16/23:02:38->23:02:41
IESA 3D Reduced 2008-06-16/23:02:50->23:02:53
a)
b)
c)
d)
V Perp (km/sec)
V Para (km/sec)
f (sec^3 / km^3 /cm^3)
1.0×10^-7
2.5×10^-8
6.3×10^-9
1.6×10^-9
4.0×10^-10
1.0×10^-10
2.5×10^-11
6.3×10^-12
1.6×10^-12
4.0×10^-13
1.0×10^-13
V perp (1000 km/s)
V par (1000 km/s)
1.000e-09
1.000e-10
1.000e-11
1.000e-12
1.000e-13
1.000e-14
1.000e-15
Max: 8.723e-08
Min: 0.000

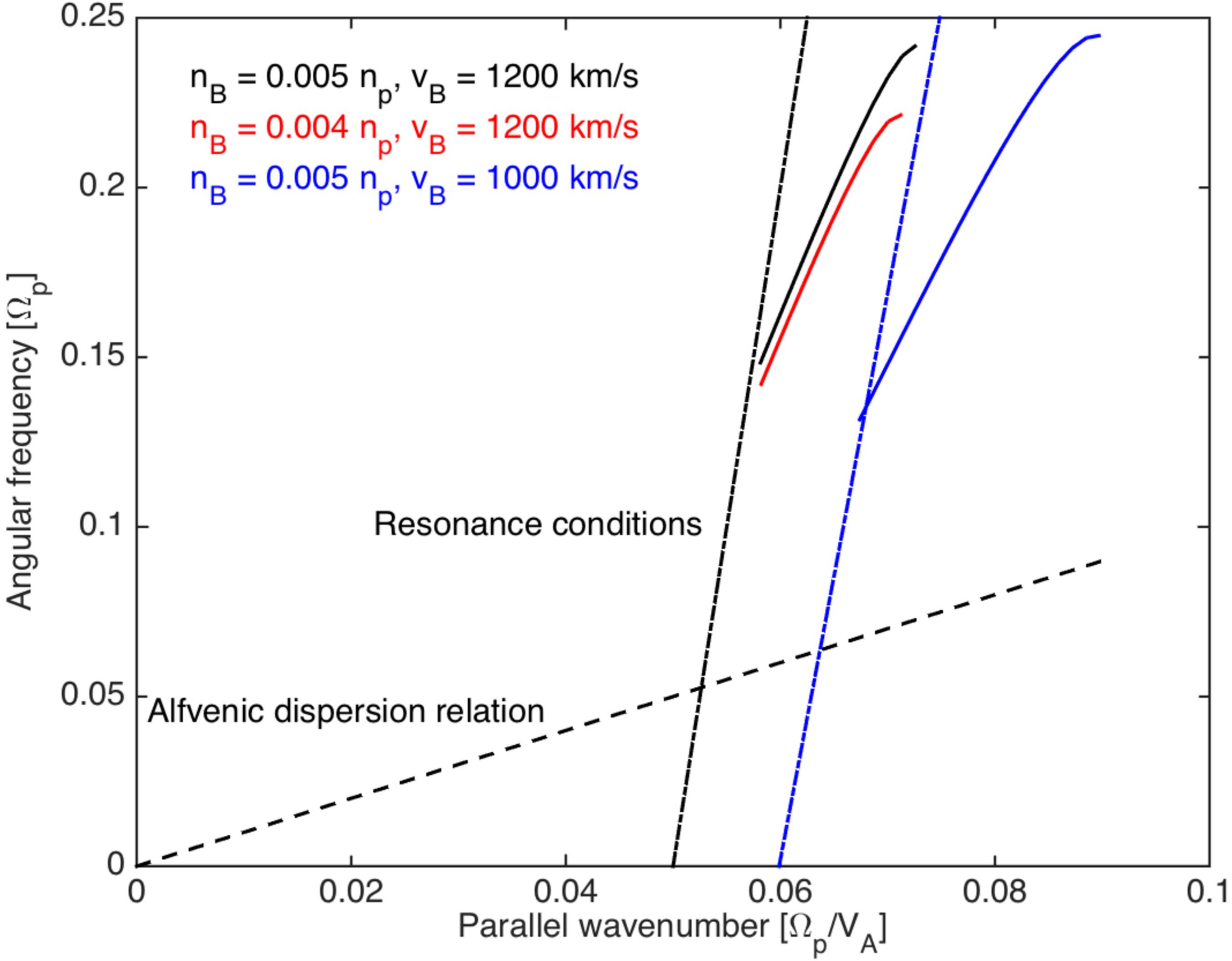

0.25
0.2
0.15
0.1
0.05
0
Angular frequency [Ω_p]
0
0.02
0.04
0.06
0.08
0.1
Parallel wavenumber [Ω_p/V_A]
n_B = 0.005 n_p, v_B = 1200 km/s
n_B = 0.004 n_p, v_B = 1200 km/s
n_B = 0.005 n_p, v_B = 1000 km/s
Resonance conditions
Alfvenic dispersion relation

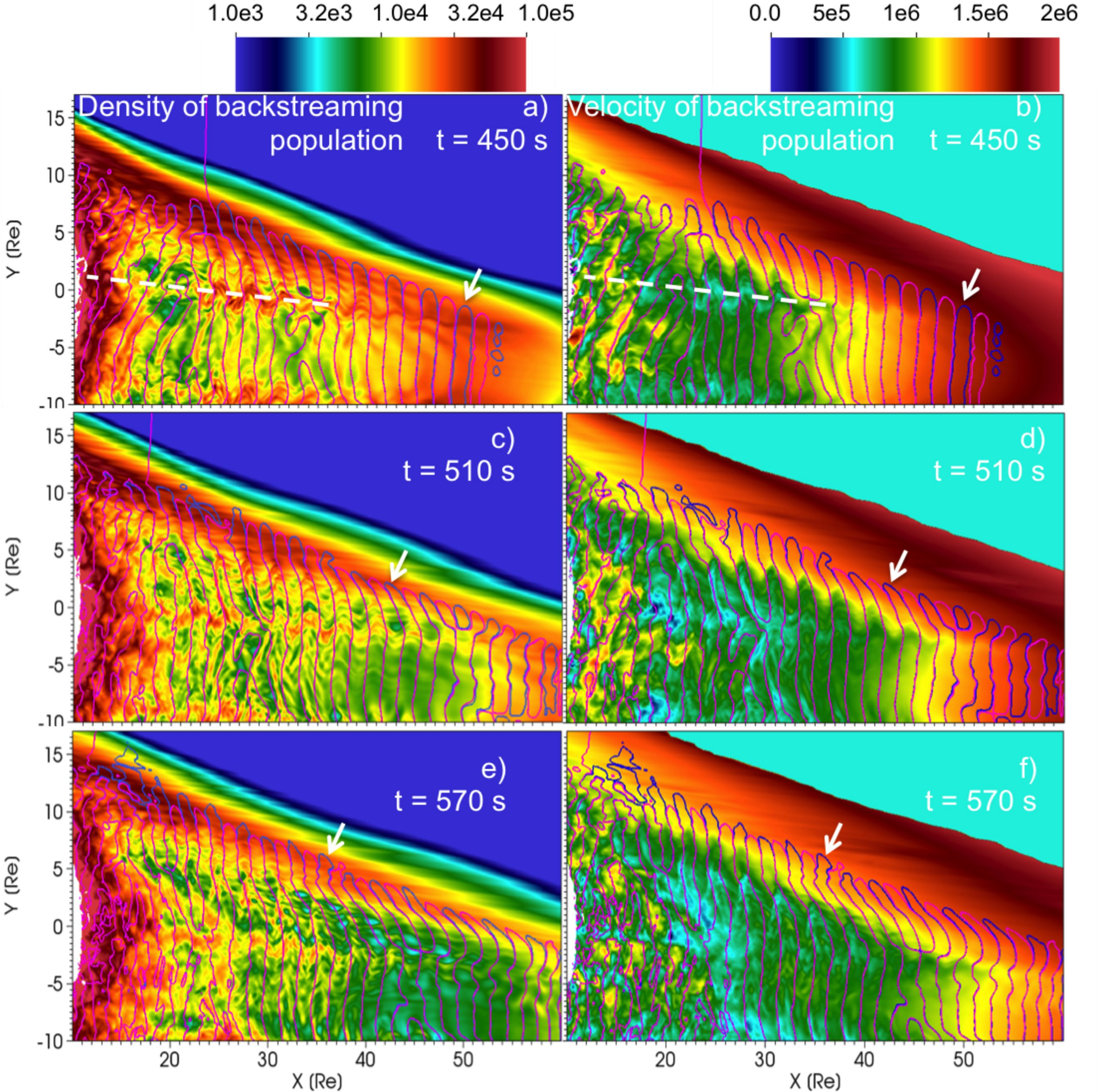
1.0e3
3.2e3
1.0e4
3.2e4
1.0e5
0.0
5e5
1e6
1.5e6
2e6
Density of backstreaming population
a) t = 450 s
Velocity of backstreaming population
b) t = 450 s
c) t = 510 s
d) t = 510 s
e) t = 570 s
f) t = 570 s
Y (Re)
X (Re)
15
10
5
0
-5
-10
20
30
40
50